Formation and evolution of Saturn's ring-moonlet system

安井，佑貴

(Degree)
博士（理学）

(Date of Degree)
2014-03-25

(Date of Publication)
2016-03-25

(Resource Type)
doctoral thesis

(Report Number)
甲第6130号

(URL)
https://hdl.handle.net/20.500.14094/D1006130

博士論文

Formation and evolution of Saturn's ring-moonlet system

(土星リング-小衛星系形成進化過程に関する
理論的研究)

平成 26 年 1 月

神戸大学大学院理学研究科

安井　佑貴

Contents

Abstract **3**

1 Introduction **4**

2 Viscosity in Planetary Rings with Spinning Self-Gravitating Particles **8**
2.1 Introduction . . . 8
2.2 Numerical Method . . . 12
2.3 Effects of Surface Friction on Viscosity in Optically Thin Rings . . . 15
2.4 Viscosity in Dense Rings . . . 20
2.5 Semianalytic Expression . . . 25
2.6 Conclusions and Discussion . . . 31

3 Gravitational Accretion of Particles onto Moonlets Embedded in Saturn's Rings **33**
3.1 Introduction . . . 33
3.2 Numerical Methods . . . 38
3.3 Test Simulation: Comparison with Three-Body Calculations . . . 43
3.4 Numerical Results: Degree of Particle Accretion . . . 48
3.4.1 Case of Partial Coverage of Moonlet Surface . . . 48
3.4.2 Case of Complete Coverage of Moonlet Surface . . . 52
3.4.3 Dependence of Degree of Particle Accretion on Radial Distance . . . 53
3.5 Effects of Ring Thickness on Particle Accretion . . . 56
3.6 Dependence on Other Parameters . . . 61
3.6.1 Particle Density . . . 61
3.6.2 Particle Size Distribution . . . 64
3.7 Conclusions and Discussion . . . 67

4 Summary **71**

Appendix **74**
Appendix A . . . 74
Appendix B . . . 75
Appendix C . . . 76
Appendix D . . . 77

Acknowledgments **79**

Bibliography **80**

Abstract

We examine viscosity in self-gravitating planetary rings in Chapter 2 and also gravitational accretion of ring particles onto moonlets in Saturn's rings in Chapter 3, using local N-body simulation.

We investigate dependence of viscosity on various parameters in detail, including effects of particles' surface friction. We find that inclusion of surface friction changes viscosity in dilute rings up to a factor of about two. In the case of self-gravitating dense rings, viscosity is increased significantly due to effects of gravitational wakes, and we find that varying restitution coefficients changes viscosity in such dense rings also by a factor of about two. However, we find that a previously obtained formula seems to overestimate viscosity in dense rings far from the central planet, where temporary gravitational aggregates form. We derive semianalytic expressions that well reproduce our numerical results for the entire range of parameters examined.

We find that gravitational accretion of ring particles onto moonlets is unlikely to occur at radial locations interior to the outer edge of the C ring, unless the density of the moonlet is much larger than that of solid water ice or non-gravitational cohesive forces play a major role. We also examine accretion process of individual particles onto moonlets in detail, and find that particle accretion onto the high-latitude regions of the moonlet surface occurs even if the vertical thickness of the ring is much smaller than the moonlet's radius. Our results suggest that larger boulders recently indicated by observations of transparent holes in the C ring are likely to be collisional shards, while propeller moonlets in the A ring would be gravitational aggregates formed by particle accretion.

Chapter 1

Introduction

Saturn's rings are composed of many icy particles. The optically thick regions of Saturn's rings are classified as main rings that consist of the A, B, and C rings (Figure 1.1). The C, B, and A rings are located in $74,500 - 92,000$ km, $92,000 - 118,000$ km, and $122,000 - 137,000$ km from the Saturn's center, respectively (e.g., Colwell et al. 2009). The optical depths of the C, B, and A rings are ~ 0.1, $1 - 5$, and ~ 0.5, respectively; they are obtained by the Voyager stellar (Holberg et al. 1982; Esposito et al. 1983, 1987) and radio occultations (Tyler et al. 1983), the ground-based observations of the occultation of the bright star 28 Sgr in July 1989 (Nicholson et al. 2000), and the Cassini stellar and radio occultations (e.g., Cuzzi et al. 2009). The vertical thickness of the main rings is ~ 10 m given by the model, under the assumption that random velocities are isotropic (Tiscareno et al. 2007). This shows that the vertical thickness of the main rings is much smaller than the width of the rings. Sizes of particles forming the main rings are estimated to be in the range of about 0.1 cm $-$ 10 m from results of the Voyager and the Cassini observations, and the ground-based observations of stellar occultations (Marouf et al. 1983; Zebker et al. 1985; French & Nicholson 2000; Cuzzi et al. 2009).

Four models for the origin of Saturn's rings have been suggested as follows: (i) the remnant from Saturn's sub-nebula disk (Pollack 1975), (ii) the collisional disruption of one or several moons (Pollack et al. 1973; Pollack 1975; Harris 1984; Charnoz et al. 2009), (iii) the tidal disruption of one or several comets (Dones 1991; Dones et

al. 2007; Charnoz et al. 2009), (iv) the stripping of the icy mantle of a Titan-sized satellite (Canup 2010). The first, the second, and the third models are unlikely to account for several characteristics such as almost pure icy composition of the rings and nonexistence of prominent rings like Saturn's rings with other giant planets. On the other hand, the fourth model seems to be able to account for the characteristics of Saturn's rings and also consistent with the recent model for the origin of regular satellites of giant planets (Canup & Ward 2002).

Dynamics of Saturn's main rings are dominated by collision and gravitational interaction between particles (Schmidt et al. 2009). The rings can be regarded as particle disks with viscosity arising from such interactions between particles, and the viscosity in Saturn's rings is an important physical parameter determining the rate of dynamical evolution and structure formation in the rings. For example, the rate of viscous spreading of the rings is determined by the viscosity (Esposito 1986; Salmon et al. 2010), and the formation of the complete and partial gaps in the rings can be described by balance between viscous spreading and gravitational scattering by an embedded body (e.g., Goldreich & Tremaine 1982; Spahn & Sremcevic 2000; Sremcevic et al. 2002).

On the other hand, there are many moonlets and satellites in Saturn's system. Detailed data on shapes and densities of small moons orbiting within or near the A ring have been obtained from observations by the Cassini spacecraft (Porco et al. 2007; Thomas 2010). While these moonlets are thought to be formed by gravitational accretion of small ring particles onto larger fragments resulting from the breakup of a bigger icy progenitor ring body (Porco et al. 2007; Charnoz et al. 2007), recent studies suggest that some of these moonlets likely formed by accretion of particles radially spreading from the outer edge of the rings, due to angular momentum transport caused by collisions and gravitational interactions between particles and satellites (Charnoz et al. 2010; Canup 2010). Also, propeller-shaped structures have been found in Cassini images of the A ring and indicate the existence of unseen

embedded moonlets with sizes between tens and thousands of meters (Figure 1.2). Some of these unseen embedded moonlets either may be collisional shards resulted from disruption of the ring's progenitor body or may have formed by accretion of ring particles onto larger fragments. Furthermore, observations by the Cassini spacecraft show that some of the small moons have prominent equatorial ridges. Thus, it is important to study viscosity and particle accretion in order to understand the formation and the evolution of Saturn's ring-moonlet system.

The viscosity in Saturn's rings has been investigated with both observational (e.g., Tiscareno et al. 2007) and theoretical (e.g., Daisaka et al. 2001) studies, the latter being only in limited cases. Comparison between observations and numerical studies can provide constrains on ring particles' properties (e.g., the restitution coefficient and the surface state of the particles) and particle size distribution. These constrains would be useful for a better understand of the formation and the evolution of the ring-moonlet system. On the other hand, in addition to observations of small moons (Porco et al. 2007), theoretical studies related to the formation of the small moons have been carried out (Porco et al. 2007; Charnoz et al. 2007; Lewis & Stewart 2009), but accretion processes have not been studied in detail. By clarifying the degree and the process of particle accretion onto moonlets in the rings, we can give constrains on the origin and evolution of the ring-satellite system.

In this doctoral thesis, we study viscosity and gravitational accretion in Saturn's rings, using local N-body simulations. In Chapter 2, performing N-body simulations for rings consisting of equal-sized particles, we examine the viscosity of planetary rings consisting of spinning, self-gravitating particles. In Chapter 3, carrying out N-body simulations of particle accretion onto a larger moonlet, we examine gravitational accretion of particles onto moonlets embedded in Saturn's rings. Our summary is presented in Chapter 4.

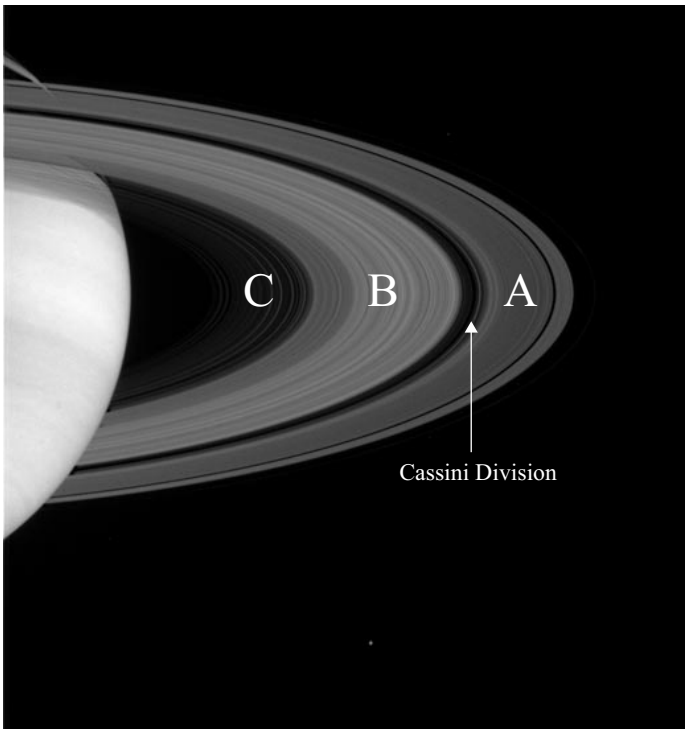

Figure 1.1: An image of Saturn's rings taken by the Cassini spacecraft. The characters "C", "B", and "A" in the image means the C ring, the B ring, and the A ring, respectively. The Cassini Division is indicated by the arrow (NASA/PIA05410-516-548).

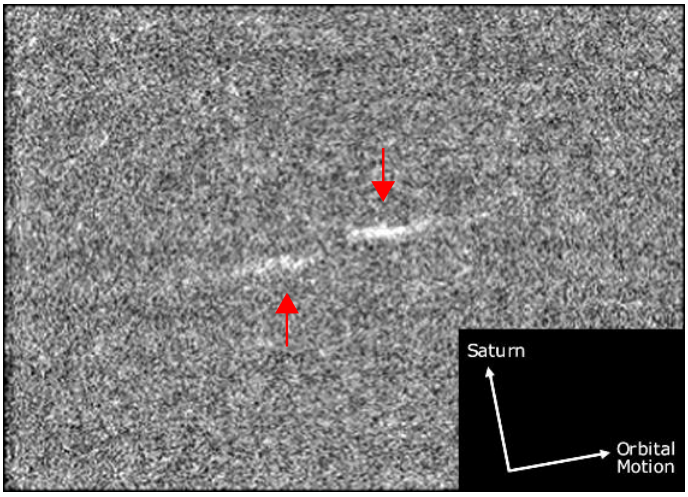

Figure 1.2: An image of the "propeller" feature in Saturn's rings obtained by the Cassini spacecraft. Red arrows indicate the "propeller" feature. The direction of Saturn and moonlet's orbital motion are illustrated at the lower right of the image (NASA/PIA07791).

Chapter 2

Viscosity in Planetary Rings with Spinning Self-Gravitating Particles

2.1 Introduction

Angular momentum transport is a key process that drives the large-scale structures of planetary rings. It determines the timescale of radial spreading, the behavior of wave structures, and the condition of gap formation in rings in the vicinity of embedded moonlets, and it is also related to the stability of dense rings (see, e.g., Goldreich & Tremaine, 1978; Stewart et al., 1984; Schmidt et al., 2009). Furthermore, recent studies show that Saturn's small moons orbiting just outside the main rings likely formed by an accretion of radially spreading particles from the outer edge of the ring (Charnoz et al., 2010; Canup, 2010); thus the spreading rate of the ring is also related to the formation of these moons.

In planetary rings, angular momentum transport is caused by collisions and gravitational interactions between particles and satellites, and the rate of the transport is expressed in terms of viscosity. In most previous works on the viscosity of planetary rings, effects of the self-gravity of the rings were either neglected or only taken into account in an approximate manner (e.g. Goldreich & Tremaine, 1978; Borderies et

The content of this chapter is an author-created, un-copyedited version of an article published in The Astronomical Journal. IOP Publishing Ltd is not responsible for any errors or omissions in this version of the manuscript or any version derived from it. The Version of Record is available online at http://dx.doi.org/10.1088/0004-6256/143/5/110.

al., 1985; Araki & Tremaine, 1986). Wisdom & Tremaine (1988) performed local simulation of planetary rings with nongravitating particles and studied their equilibrium properties, including viscosity. In addition to the local component of angular momentum transport due to particle radial random motion examined by Goldreich & Tremaine (1978), Wisdom & Tremaine (1988) also evaluated the non-local component due to collision. They found that the nonlocal component dominates the viscosity in dense rings, and they confirmed that the values of the viscosity agree well with the result of Araki & Tremaine (1986). They also examined effects of self-gravity in an approximate manner by enhancing the vertical frequency of particle orbital motion, and they found that the viscosity is enhanced by a factor of five. Richardson (1994) calculated ring viscosity using N-body simulation of self-gravitating rings, but did not examine the angular momentum transport due to gravitational interactions between particles.

On the other hand, Daisaka et al. (2001) studied viscosity in self-gravitating rings using local N-body simulation. In addition to the local and nonlocal components studied by Wisdom & Tremaine (1988), Daisaka et al. (2001) calculated the gravitational component of viscosity based on the formulation of Takeda & Ida (2001), who studied angular momentum transport in proto-lunar disks. Takeda & Ida (2001) and Daisaka et al. (2001) found that the viscosity is strongly enhanced when particle disks become gravitationally unstable and gravitational wakes are formed. From their numerical results, Daisaka et al. (2001) derived a formula of the viscosity in self-gravitating dense rings given by $\nu \sim CG^2\Sigma^2/\Omega^3$, where G is the gravitational constant, Σ and Ω are the surface density and angular velocity of the ring, respectively, and C is a correction factor that depends on the ratio of the Hill radius of the particles to their physical size (see Section 2.5). However, the range of parameters studied by Daisaka et al. (2001) was somewhat limited; for example, they did not examine viscosities in dense rings far from the planet, where temporary gravitational aggregates can form. Also, they assumed that particles are smooth spheres, and did

not examine the effects of surface friction of particles on the viscosity.

Spins of ring particles arise as a natural outcome of oblique impacts between particles with surface friction. Spin rate of ring particles is an important parameter in modeling thermal emission from Saturn's rings, and it has been studied in detail, using analytic calculation, three-body orbital integration, and N-body simulation (Salo, 1987; Richardson, 1994; Ohtsuki, 2005; Ohtsuki & Toyama, 2005; Ohtsuki, 2006a,b; Morishima & Salo, 2006). These studies show that the spin period of the particles is on the order of their orbital period in rings of equal-sized particles, while small particles spin faster than larger ones when size distribution is included. Considering energy balance between viscous gain and dissipation due to an inelastic collision with surface friction, Morishima & Salo (2006) examined the effects of particle surface friction on viscosity in rings consisting of non-gravitating particles, but such effects on the viscosity in self-gravitating rings were not studied.

On the other hand, Tanaka et al. (2003) derived a new formulation for the calculation of the total viscosity (i.e., the sum of the local, nonlocal, and gravitational components) in particle disks. Under Hill's approximations in the three-body problem, they derived an expression of angular momentum flux in terms of the changes of orbital elements of constituent particles due to mutual collisions and gravitational interactions. In the case of planetary rings with low optical depth, they showed that viscosity can be evaluated by three-body orbital integration. They also derived a formula to calculate viscosity in dense rings using N-body simulation. In this case, viscosity in rings in a quasisteady state can be obtained from energy dissipation at inelastic collisions between particles (see Section 2.2). In the case of rings with the effect of vertical overall self-gravity, Salo et al. (2001) also found agreement between viscous heating and energy dissipation due to inelastic collision using N-body simulation. Tanaka et al. (2003) confirmed that viscosities in planetary rings calculated using their new formula agree with those obtained by the method used by Daisaka et al. (2001). This new method of viscosity calculation can also be used in the case

of particles with surface friction, and the method is convenient when investigating detailed parameter dependence of the total viscosity of the rings.

In the present work, we examine the viscosity of planetary rings consisting of spinning, self-gravitating particles. Using an N-body simulation code similar to the one developed by and used in Daisaka & Ida (1999) and Daisaka et al. (2001) and on the basis of the above viscosity calculation formula derived by Tanaka et al. (2003), we calculate ring viscosity for a wide range of parameters, including cases of particles with surface friction. We also examine viscosities in dense rings far from the central planet, where temporary gravitational aggregates can form. In Section 2.2, we describe our numerical methods. Numerical results of our N-body simulation are presented in Sections 2.3 and 2.4. First, in Section 2.3, we describe the effects of surface friction on viscosity in rings with low optical depth. Then, we show results for dense rings of spinning self-gravitating particles in Section 2.4. In Section 2.5, we derive semianalytic expressions of ring viscosity based on our numerical results. Our conclusions are summarized in Section 2.6.

2.2 Numerical Method

We adopt the method of local N-body simulation (e.g. Wisdom & Tremaine, 1988; Richardson, 1994; Salo, 1995; Daisaka & Ida, 1999; Ohtsuki & Emori, 2000; Daisaka et al., 2001), and use a code based on Daisaka & Ida (1999) and Daisaka et al. (2001). We erect a rotating Cartesian coordinate system with origin at the center of the square simulation cell that moves on a circular orbit with a semimajor axis a_0 at the Keplerian angular velocity $\Omega = (GM_{\rm c}/a_0^3)^{1/2}$ ($M_{\rm c}$ is the mass of the central planet). The x-axis points radially outward, the y-axis points in the direction of the orbital motion, and the z-axis is normal to the equatorial plane. In this case, the equations of motion of particle i are written as

$$\begin{aligned}
\ddot{x}_i &= 2\dot{y}_i\Omega + 3x_i\Omega^2 + \sum_{j\neq i}^{N} \frac{Gm_j\,(x_j - x_i)}{r_{ij}^3} \\
\ddot{y}_i &= -2\dot{x}_i\Omega + \sum_{j\neq i}^{N} \frac{Gm_j\,(y_j - y_i)}{r_{ij}^3} \\
\ddot{z}_i &= -z_i\Omega^2 + \sum_{j\neq i}^{N} \frac{Gm_j\,(z_j - z_i)}{r_{ij}^3}
\end{aligned} \tag{2.1}$$

where $r_{ij} = \left[(x_i - x_j)^2 + (y_i - y_j)^2 + (z_i - z_j)^2\right]^{1/2}$, N is the particle number, m_j is the mass of particle j, and the last terms on the right-hand side of Equation (2.1) denote gravitational forces between particles. We directly calculate the gravitational forces between particles using GRAPE-7, which is a special-purpose hardware for calculating gravitational forces, and orbits of particles are integrated with the second-order leapfrog method. In the present work, we assume that all particles have identical sizes of 1m radius.

When collisions between particles are detected, velocity changes are calculated based on the hard-sphere model including surface friction (e.g. Salo, 1987; Richardson, 1994; Ohtsuki & Toyama, 2005). Velocity changes are described in terms of the normal and tangential restitution coefficients, $\varepsilon_{\rm n}$ and $\varepsilon_{\rm t}$, where $0 \leq \varepsilon_{\rm n} \leq 1$ and $-1 \leq \varepsilon_{\rm t} \leq 1$. (Perfectly smooth spheres have $\varepsilon_{\rm t} = 1$.) Let the normal and the tan-

gential components of the relative velocity ($\boldsymbol{v}$) of colliding particles to the tangent plane be $\boldsymbol{v}_{\rm n}$ and $\boldsymbol{v}_{\rm t}$, respectively, and the normal and the tangential components of the relative velocity of the two contacting points at the time of impact be $\boldsymbol{u}_{\rm n}$ and $\boldsymbol{u}_{\rm t}$, respectively. Then, the normal and the tangential components of the relative velocity of the two contacting points after impact are given as

$$\begin{aligned} \boldsymbol{u}'_{\rm n} &= \boldsymbol{v}'_{\rm n} = -\varepsilon_{\rm n}\boldsymbol{v}_{\rm n}, \\ \boldsymbol{u}'_{\rm t} &= \varepsilon_{\rm t}\boldsymbol{u}_{\rm t}. \end{aligned} \tag{2.2}$$

Using these relations, we calculate changes in velocities and rotation the rates of colliding particles (Appendix A). In the present study, we assume that $\varepsilon_{\rm t}$ is constant and examine the dependence of viscosity on $\varepsilon_{\rm t}$. As for the normal restitution coefficient, in addition to cases with constant $\varepsilon_{\rm n}$'s, we also examine cases with the velocity-dependent coefficient based on laboratory impact experiments (Bridges et al., 1984), which is given as

$$\varepsilon_n\left(v\right) = \min\left\{0.32\left(v/v_c\right)^{-0.234}, \quad 1\right\} \tag{2.3}$$

where $v_c = 1\,{\rm cm\,s^{-1}}$.

We calculate ring viscosities based on the formulation derived by Tanaka et al. (2003). Deriving an expression for angular momentum flux in terms of changes in particle orbital elements and assuming a quasisteady state in a local ring region, Tanaka et al. (2003) showed that the averaged viscosity in the ring region can be obtained by calculating energy dissipation due to inelastic collisions using N-body simulation. In the case of N-body simulation using a square simulation cell of width L, the viscosity averaged over the cell and a time interval T is written as (Tanaka et al., 2003)

$$\nu \;=\; \frac{4}{9\Omega^2\Sigma T L^2}\sum_{j}^{\rm inside}\sum_{\substack{k\\ b_k>b_j}}^{\rm all}\sum_{\rm all\ collisions}\Delta E_{{\rm col},jk}, \tag{2.4}$$

where Σ is the averaged surface density and $\Delta E_{{\rm col},jk}\,(>0)$ is an amount of energy dissipated at a collision between particle j and particle k. $\Delta E_{{\rm col},jk}$ can be calculated, for example, from the change of the orbital elements for the relative motion of

particles due to a collision (Appendix B). The first summation is taken over particle j whose guiding center is inside the simulation cell, while the second summation is over particle k, which have a semimajor axis of the guiding center (b) larger than that of particle j. The above expression can also be obtained by assuming a balance between energy loss due to inelastic collisions and the viscous gain due to the shear motion (Tanaka et al. 2003; see also Salo et al. 2001).

In the case of nongravitating rings or self-gravitating rings with low optical depth, $N \sim 10^3$ or an even smaller number of particles is sufficient to examine such equilibrium properties, e.g., velocity dispersion. However, in the case of self-gravitating dense rings, a sufficiently large simulation cell (thus, a sufficiently large number of particles) should be used to accurately obtain various dynamical quantities (Salo, 1995). Following Salo (1995), we set the size of the simulation cell so that $L \geq 4\lambda_{\rm cr}$, where $\lambda_{\rm cr} = 4\pi^2 G\Sigma/\Omega^2$ is the critical wavelength for axisymmetric gravitational instability. We performed simulations for sufficiently long time periods to achieve a quasisteady state; these were typically at least 20-50$T_{\rm K}$ ($T_{\rm K}$ is the Keplerian orbital period) for dense rings ($10T_{\rm K}$ for $\tau = 1$ and $r_{\rm h} = 1$, where $r_{\rm h}$ is defined by Equation (2.5)), and still longer periods in the case of dilute rings. The time average for calculating viscosities from Equation (2.4) is carried out after a quasisteady state is achieved.

2.3 Effects of Surface Friction on Viscosity in Optically Thin Rings

In this section, we first show results for nongravitating rings. Then, we describe in detail results for self-gravitating rings with a low optical depth. Numerical results for self-gravitating dense rings will be presented in Section 2.4.

Figure 2.1 shows numerical results for viscosity in the case of nongravitating rings as a function of optical depth. First, to confirm the validity of our code for N-body simulation and viscosity calculation, we compare our results with Wisdom & Tremaine (1988) by performing simulations for the same parameters, i.e., smooth particles ($\varepsilon_{\rm t} = 1$) with $\varepsilon_{\rm n} = 0.5$. In Figure 2.1(a), the crosses represent results from Wisdom & Tremaine (1988), and the line shows our results. We find excellent agreement between the two results. Figure 2.1(b) shows our numerical results for the velocity-dependent normal restitution coefficient given by Equation (2.3) with $\varepsilon_{\rm t} = 1$, 0.5, and 0. We find that the dependence of viscosity on the value of $\varepsilon_{\rm t}$ is different between the low and high optical depth cases, and this difference is related to the behavior of particle random velocity. In the case of low optical depth, random velocity is somewhat reduced with the increasing strength of surface friction (Salo, 1987; Ohtsuki & Toyama, 2005), and the reduced radial excursion of particles lowers the rate of angular momentum transport and viscosity (Goldreich & Tremaine, 1978). On the other hand, in the case of high optical depth, the dependence of random velocity on τ or $\varepsilon_{\rm t}$ becomes rather weak (Wisdom & Tremaine, 1988). In this case, viscosity becomes larger with decreasing $\varepsilon_{\rm t}$, because viscous heating increases to balance the additional energy dissipation due to surface friction.

Next, we examine the case of self-gravitating rings with a low optical depth. The relative importance of self-gravity to mutual collision between particles depends on the relative size of the Hill radius of the particles to their physical size (Ohtsuki, 1993, 1999; Salo, 1995; Daisaka et al., 2001). In the case of rings of equal-sized particles (mass m, radius R, internal density ρ) at a distance a_0 from the planet, the ratio of

the mutual Hill radius $R_{\rm H}\left(=a_0\,(2m/3M_{\rm c})^{1/3}\right)$ of colliding particles to the sum of their radii is written as (Daisaka et al., 2001)

$$\begin{aligned} r_{\rm h} &= R_{\rm H}/(2R) \\ &= 0.82\left(\frac{M_{\rm c}}{5.7\times10^{29}\,{\rm g}}\right)^{-1/3}\left(\frac{\rho}{0.9\,{\rm g\,cm^{-3}}}\right)^{1/3}\left(\frac{a_0}{10^{10}\,{\rm cm}}\right). \end{aligned} \tag{2.5}$$

Figure 2.2 shows the plots of $r_{\rm h}$ as a function of the distance from Saturn, for several values of ρ. When $\rho = 0.9\,{\rm g\,cm^{-3}}$, $r_{\rm h} = 0.5$, 0.71, and 1 (see, e.g., Figure 2.3) correspond to $a/10^{10}\,{\rm cm} = 0.61$, 0.87, and 1.22, respectively. However, if $\rho = 0.5\,{\rm g\,cm^{-3}}$, the above three values of $r_{\rm h}$ correspond to $a/10^{10}\,{\rm cm} = 0.74$, 1.05, and 1.48, respectively. Although the actual physical properties of ring particles are poorly known, comparisons between the observations and dynamical studies suggest that it is likely they are underdense (e.g., Schmidt et al., 2009).

Figure 2.3 shows the dependence of viscosity and random velocity on $\varepsilon_{\rm n}$ for low optical depth rings ($\tau = 0.01$) with four different values of $r_{\rm h}$, including the nongravitating case ($r_{\rm h} = 0$). Figure 2.3(b) confirms the dependence of random velocity on $\varepsilon_{\rm n}$ and $r_{\rm h}$ (or the distance from the planet for a given density) obtained by previous studies (e.g., Salo, 1995; Ohtsuki, 1999). In the case of no or weak gravity, random velocity is determined by a mutual collision and the equilibrium random velocity increases with increasing $\varepsilon_{\rm n}$, while the $\varepsilon_{\rm n}$-dependence becomes weak in the case of larger $r_{\rm h}$, where gravitational encounters between particles become important. More importantly, the random velocity significantly increases with increasing $r_{\rm h}$, i.e., the increasing effect of gravitational encounters. The $\varepsilon_{\rm n}$-dependence of viscosity shown in Figure 2.3(a) is similar to but somewhat weaker than that of random velocity. However, we find that the $r_{\rm h}$-dependence of the viscosity is similar to that of random velocity, indicating that viscosity in self-gravitating rings with low optical depth can be roughly expressed in terms of random velocity, as in the case of the dilute nongravitating rings discussed above.

Figure 2.4 shows the dependence of viscosity and random velocity on $\varepsilon_{\rm t}$ in self-gravitating rings with low optical depth. We also show the results for the nongravi-

tating case ($r_{\rm h} = 0$) for comparison. The curves for the random velocity in the case of weak gravity ($r_{\rm h} = 0.5$) are very close to those for the nongravitating case. In these cases, energy dissipation due to surface friction is most effective at $\varepsilon_{\rm t} = 0$; thus, the random velocity becomes the smallest at $\varepsilon_{\rm t} \simeq 0$ (Morishima & Salo, 2006). Then, the reduced radial excursion of particles results in the reduction of viscosity (Figure 2.4(a)), as mentioned above. The behavior in the case of $r_{\rm h} = 0.71$ is similar, although the $\varepsilon_{\rm t}$-dependence of the viscosity seems rather weak. In the case of $r_{\rm h} = 1$, on the other hand, gravitational encounters between particles play a major role in determining random velocity. As a result, the random velocity becomes almost independent of $\varepsilon_{\rm t}$. In this case, impact velocity also becomes nearly independent of $\varepsilon_{\rm t}$, and energy dissipation at the collision is the largest when surface friction is the strongest, i.e., at $\varepsilon_{\rm t} \simeq 0$. Therefore, the viscosity in the case of $r_{\rm h} = 1$ becomes larger when $\varepsilon_{\rm t} \simeq 0$ by a factor of about two compared with the case of smooth particles ($\varepsilon_{\rm t} = 1$). Here, we emphasize that both viscosity and random velocity increase with increasing $r_{\rm h}$ and, if we neglect the above rather weak $\varepsilon_{\rm t}$-dependence, viscosity in self-gravitating rings with low optical depth seems to be expressed in terms of random velocity (Section 2.5).

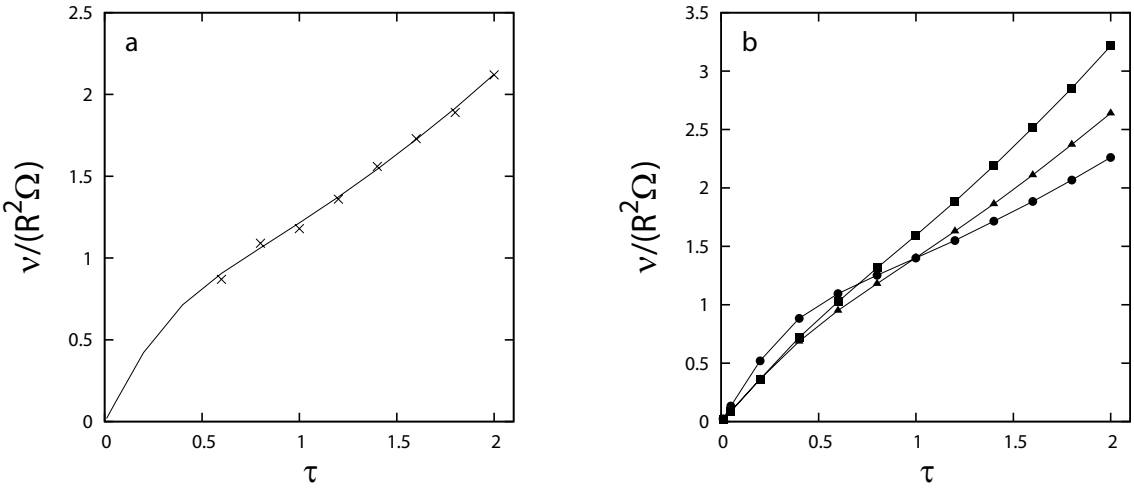

Figure 2.1: Viscosity in the case of nongravitating rings as a function of optical depth. (a) Solid line shows our numerical results with $\varepsilon_{\rm n} = 0.5$ and $\varepsilon_{\rm t} = 1$, and the crosses are those obtained by Wisdom & Tremaine (1988) for the same parameters. (b) Our numerical results with the velocity-dependent normal restitution coefficient $\varepsilon_{\rm n}(v)$ given by Equation (2.3), with $\varepsilon_{\rm t} = 1$ (circles), 0.5 (triangles), and 0 (squares) (from Yasui et al. 2012).

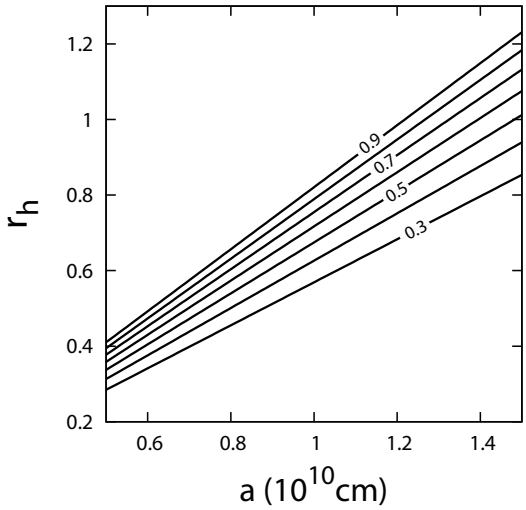

Figure 2.2: Dependence of $r_{\rm h}$ on the distance from Saturn for the case of equal-sized particles and several values of particle internal density. Cases for $\rho = 0.3$-0.9 g cm^{-3} are shown with an interval of 0.1 g cm^{-3} (from Yasui et al. 2012).

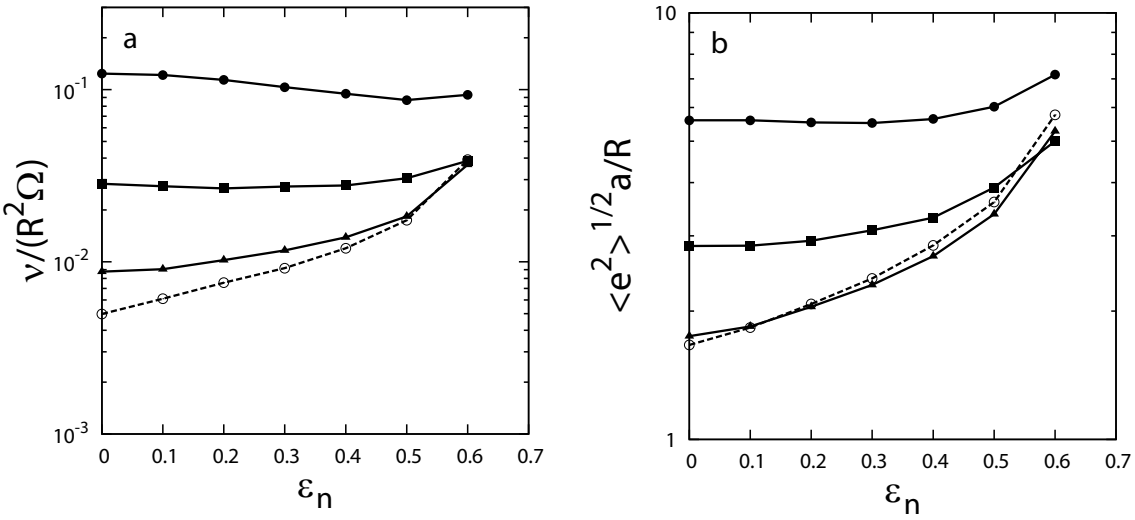

Figure 2.3: (a) Dependence of viscosity on $\varepsilon_{\rm n}$ for $r_{\rm h} = 0$ (dashed line with open circles), 0.5 (triangles), 0.71 (squares), and 1 (solid circles) $\left(\tau = 0.01,\ \varepsilon_{\rm t} = 1,\ N = 10^3\right)$. (b) Same as (a), but for random velocity (from Yasui et al. 2012).

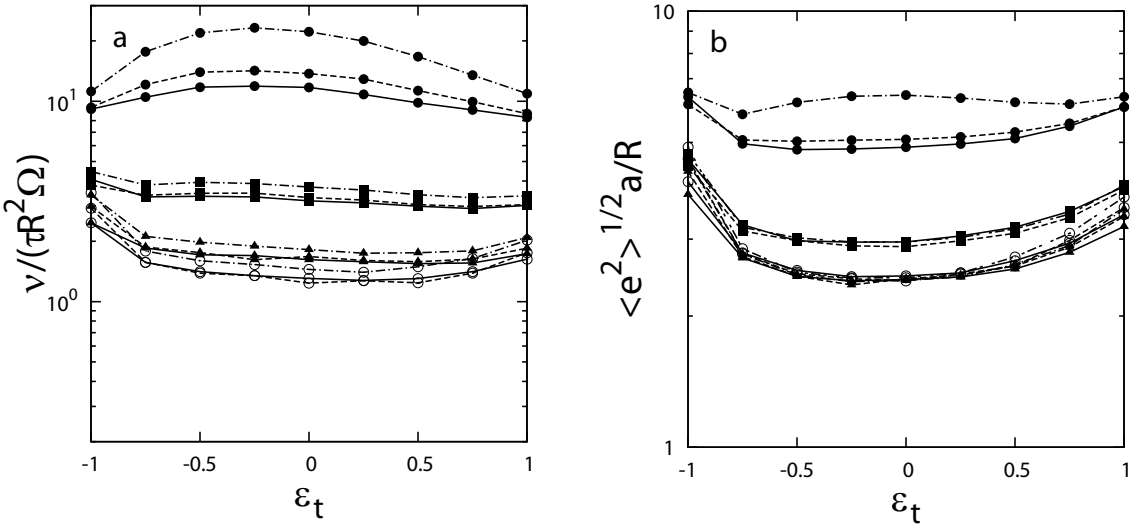

Figure 2.4: Scaled viscosity and random velocity as a function of $\varepsilon_{\rm t}$ obtained from N-body simulation $\left(N = 10^3\right)$. Symbols represent the results for different values of $r_{\rm h}$; $r_{\rm h} = 0$ (open circles), 0.5 (triangles), 0.71 (squares), and 1 (solid circles), respectively. Each line type represents a corresponding combination of τ and $\varepsilon_{\rm n}$ used in the simulation; solid lines, dashed lines, and dot-dashed lines represent $\tau = 0.01$ with $\varepsilon_{\rm n} = \varepsilon_{\rm n}\,(v)$, $\tau = 0.01$ with $\varepsilon_{\rm n} = 0.5$, and $\tau = 0.05$ with $\varepsilon_{\rm n} = 0.5$, respectively (from Yasui et al. 2012).

2.4 Viscosity in Dense Rings

Next, we examine the case of dense, self-gravitating rings. First, we show results for smooth particles, to compare with cases with surface friction shown later. The solid line with marks in Figure 2.5(a) shows the plots of the viscosity obtained by our N-body simulation as a function of optical depth ($r_{\rm h} = 0.82,\ \varepsilon_{\rm n} = 0.5,\ \varepsilon_{\rm t} = 1$). In the case of low optical depth, viscosity is proportional to the optical depth, because angular momentum is transferred via successive binary collisions and gravitational encounters between particles, and the frequency of interactions is proportional to the particle surface number density. The coefficient of proportionality in the case of self-gravitating rings with low optical depth can be obtained from results of three-body orbital integration (Tanaka et al., 2003). In this case, equilibrium random velocity for given parameters (i.e., $r_{\rm h}$, $\varepsilon_{\rm n}$, and $\varepsilon_{\rm t}$) is first calculated by solving the velocity evolution equation with the velocity stirring rates obtained from the three-body orbital integration (Ohtsuki, 1999). Then, we evaluate the coefficient for the viscosity for this equilibrium velocity by also using the results of the three-body orbital integration, and the result is shown in Figure 2.5(a) with the dotted line. We find that the results obtained by the two different methods perfectly agree with each other in the case of low optical depth. On the other hand, the results of N-body simulation deviate from the three-body results for $\tau \gtrsim 0.2$. This is because the viscosity is dominated by the angular momentum transfer related to the gravitational torques exerted by the wake structures formed in such dense, self-gravitating rings (Figure 2.6; Daisaka et al., 2001).

In addition to the smooth particles case, we show the results of our N-body simulation for self-gravitating rings of particles with surface friction in Figure 2.5(b). We find that the overall behavior in the case with surface friction is similar to the case with smooth particles. Figure 2.5(b) shows the numerical results for four combinations of $\varepsilon_{\rm n}$ (0.5 or $\varepsilon_{\rm n}(v)$ given by Equation (2.3)) and $\varepsilon_{\rm t}$ (1, 0.5, or 0). Figure 2.5(c) is the same as Figure 2.5(b), but the viscosity values are scaled by those in

the case of $\varepsilon_{\rm n} = 0.5$ and $\varepsilon_{\rm t} = 1$, to facilitate a comparison among the four cases. We note that the viscosity values change systematically when the restitution coefficients are varied. In dense rings where gravitational wakes are formed, the balance between gravitational heating by wakes and inelastic dissipation leads to a quasisteady state with $Q \simeq$ 1-2, where Q is the Toomre parameter, and the dependence of the particle random velocity (thus their impact velocity) on elastic properties is rather weak (Salo, 1995). In this case, the average energy dissipation rate is larger when the effect of the surface friction is stronger, resulting in somewhat larger viscosity values (Figures 2.5(b) and (c)). We also note that the slope of the curve for the case with $\varepsilon_{\rm n}\,(v)$ in Figure 2.5(b) becomes somewhat steeper at $\tau \gtrsim 0.2$. This is because the increased impact velocities at a larger optical depth results in the increase in energy dissipation and viscosity in the case with the velocity-dependent restitution coefficient. Figure 2.5(c) shows that varying restitution coefficients can change the viscosity in dense self-gravitating rings by a factor of about two.

Figure 2.7 shows the τ-dependence of viscosity for various values of $r_{\rm h}$, including the nongravitating case ($r_{\rm h} = 0$; dashed line), with surface friction and the velocity-dependent $\varepsilon_{\rm n}$. As in the case shown in Figure 2.5, viscosity in dilute rings is proportional to the optical depth, while it significantly increases at large τ in the case with self-gravity. We confirmed that Q takes on values smaller than 2 - 3 when viscosities begin to deviate from the linear τ-dependence. The deviation begins at $\tau \sim 0.1$ in the case of strong gravity ($r_{\rm h} = 1$). On the other hand, in the case of weak gravity ($r_{\rm h} = 0.5$), the deviation is very small and the viscosity values are close to those for the non-gravitating case even at $\tau \simeq 1$. In this case of weak self-gravity, the tendency of wake formation is not strong even at $\tau \simeq 1$ (Figure 2.8). The wake structures for $\tau = 1$ become notable with increasing $r_{\rm h}$; even temporary aggregates can form in the case of $r_{\rm h} = 1$.

The τ-dependence of viscosity, often expressed in terms of $\beta \equiv d\ln\nu/d\ln\tau$, is related to the condition for the onset of viscous overstability in dense rings; Salo et

al. (2001) found that $\beta > \beta_{\rm cr} \sim 1$ as a rough condition for the onset of overstability. In the high-τ regime where viscosity is enhanced by the effect of self-gravity, the slope of the curves shown in Figure 2.7 seems to change with increasing optical depth. For example, in the case of $r_{\rm h} = 0.82$, viscosity increases more rapidly than the $\nu \propto \tau^2$ dependence (i.e. $\beta > 2$) when the effect of gravitational wakes becomes important at $\tau \simeq 0.2$-0.3, then $\beta \simeq 2$ at $\tau \simeq 0.5$-1. Similar behavior can be seen in the cases of $r_{\rm h} = 0.71$ and 1. Figure 14.8 (upper right panel) of Schmidt et al. (2009), drawn by Heikki Salo, shows the change of β in the case of $r_{\rm h} = 0.82$ in more detail, where β increases from 1 to about 3 as τ increases from 0.1 to 0.5, then decreases to about 2 as τ further increases to $\sim$1. In the range of parameters shown here and studied in other works (e.g., Daisaka et al., 2001; Schmidt et al., 2009), we find that $1 \lesssim \beta \lesssim 3$ in self-gravitating dense rings, satisfying the condition for the onset of overstability. Simulations of dense rings for much longer periods with a larger simulation cell are necessary for a more detailed study of viscous overstability (Daisaka et al., 2001; Salo et al., 2001).

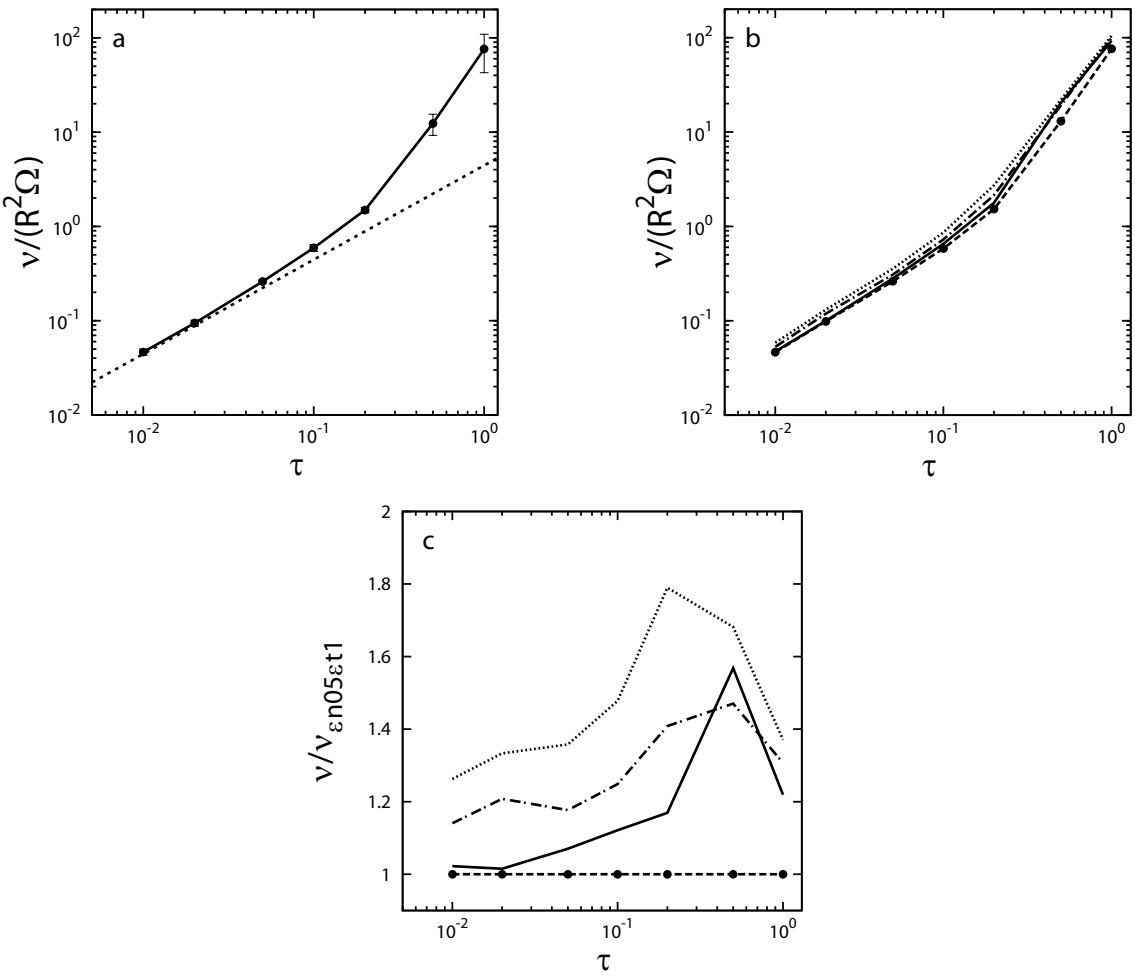

Figure 2.5: (a) Scaled viscosity as a function of optical depth. Solid line represents results of N-body simulation, while the dotted line was drawn using a coefficient evaluated by the three-body orbital integration (i.e., $\nu/\left(R^2\Omega\right) = 4.44\tau$). In both cases, $r_{\rm h} = 0.82$ (corresponding to $a = 10^{10}\,{\rm cm}$ in Saturn's rings if $\rho = 0.9\,{\rm g\,cm^{-3}}$), $\varepsilon_{\rm n} = 0.5$, and $\varepsilon_{\rm t} = 1$ are used. In the N-body simulations, $N = 5000$ for $\tau \leq 0.5$, while $N = 36,000$ is used for $\tau = 1$ so that $L/\lambda_{\rm cr} \simeq 4$. (b) Same as (a), but results of N-body simulation for four different combinations of $\varepsilon_{\rm n}$ and $\varepsilon_{\rm t}$ are shown. $\varepsilon_{\rm n} = 0.5$ and $\varepsilon_{\rm t} = 1$ (dashed line with circles); $\varepsilon_{\rm n} = 0.5$ and $\varepsilon_{\rm t} = 0.5$ (dot-dashed line); $\varepsilon_{\rm n} = 0.5$ and $\varepsilon_{\rm t} = 0$ (dotted line); and $\varepsilon_{\rm n} = \varepsilon_{\rm n}\,(v)$ and $\varepsilon_{\rm t} = 0.5$ (solid line). (c) Same as (b), but the viscosity values are scaled by those for the case of $\varepsilon_{\rm n} = 0.5$ and $\varepsilon_{\rm t} = 1$ (from Yasui et al. 2012).

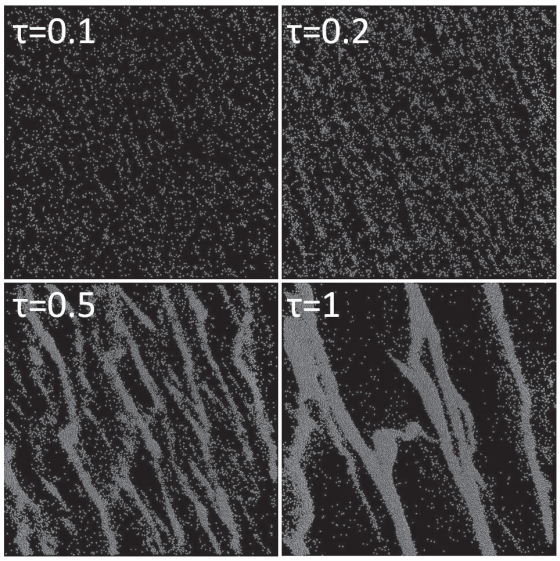

Figure 2.6: Snapshots of the spatial distribution of particles for simulations with four different values of τ ($r_{\rm h} = 0.82$, $\varepsilon_{\rm n} = 0.5$, $\varepsilon_{\rm t} = 1$). Particle radius is 1m, and the size of the simulation cell for the cases shown here is about 340m. Note that in our simulations the size of the simulation cell is varied depending on τ and $r_{\rm h}$. Here (and in Figure 2.8) we show snapshots with a common size of the simulation cell to facilitate comparison between the panels (from Yasui et al. 2012).

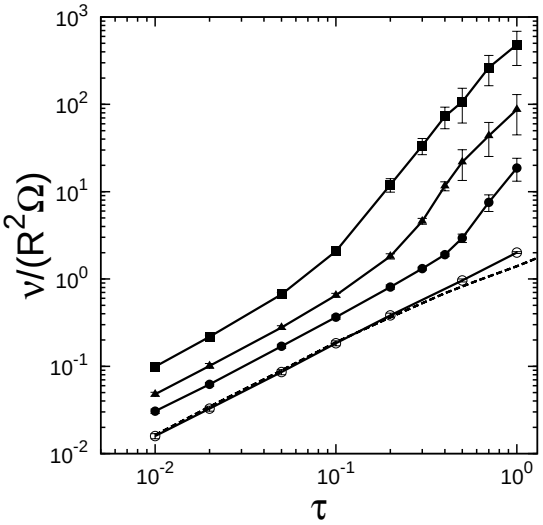

Figure 2.7: Dependence of viscosity on τ for five values of $r_{\rm h}$ ($\varepsilon_{\rm n} = \varepsilon_{\rm n}(v)$, $\varepsilon_{\rm t} = 0.5$). Solid lines with marks represent results of N-body simulation for $r_{\rm h} = 0.5$ (open circles), 0.71 (solid circles), 0.82 (triangles), and 1 (squares). Dashed line represents the nongravitating case ($r_{\rm h} = 0$). In these simulations, $N = 5000$ for cases of low optical depth, weak gravity (small $r_{\rm h}$), or both. The particle number is increased in the cases of dense rings with self-gravity, so that $L/\lambda_{\rm cr} \geq 4$ is satisfied. For example, in the case of $\tau = 1$, particle numbers are $N = 5000$, 15,000, 36,000, 115,800 for $r_{\rm h} = 0.5$, 0.71, 0.82, 1, respectively (from Yasui et al. 2012).

2.5 Semianalytic Expression

On the basis of our numerical results presented above, here we derive a semianalytic expression for viscosity in rings of equal-sized particles. As we discussed above, ring viscosity depends on various parameters. We have shown that varying restitution coefficients can change ring viscosity for a given τ and $r_{\rm h}$ by a factor of about two. On the other hand, ring viscosity changes by orders of magnitude when τ, $r_{\rm h}$, or both are varied. In the following, we will use our numerical results in the case of $\varepsilon_{\rm n} = \varepsilon_{\rm n}(v)$ and $\varepsilon_{\rm t} = 0.5$ and derive semianalytic expressions that approximately reproduce the dependence of these results on τ and $r_{\rm h}$.

First, in the case of low optical depth, viscosity is determined by particle velocity dispersion c, as shown by Goldreich & Tremaine (1978) for nongravitating rings. We also discussed this in Section 2.3 for the case of self-gravitating rings. Viscosity in this case can be written as

$$\nu_{\rm low} = \alpha c^2 \tau / \Omega, \tag{2.6}$$

where α is a constant. In optically thin rings, the velocity dispersion c can be written as (e.g. Salo, 1995; Ohtsuki, 1999)

$$c \sim \max\left\{2R\Omega,\ \sqrt{2Gm/R}\right\}, \tag{2.7}$$

depending on either inelastic collisions or gravitational encounters dominate particle velocity evolution. Substituting Equation (2.7) into Equation (2.6), viscosity in low optical depth rings can be expressed in terms of optical depth, distance from the planet, and particle internal density, as

$$\frac{\nu_{\rm low}}{R^2\Omega} \sim \max\left\{4,\ 15 \times \left(\frac{\rho}{0.9\,{\rm g\,cm^{-3}}}\right)\left(\frac{a}{10^{10}\,{\rm cm}}\right)^3\left(\frac{M_{\rm c}}{5.7\times10^{29}\,{\rm g}}\right)^{-1}\right\}\alpha\tau. \tag{2.8}$$

We find that $\alpha \sim 0.35$ from the comparison with our numerical results, which is roughly consistent with the nongravitating case (Goldreich & Tremaine, 1978).

Next, we examine the case of high optical depth. From a dimensional analysis (see also Lynden-Bell & Kalnajs, 1972; Ward & Cameron, 1978), Daisaka et al. (2001)

argued that the viscosity in dense rings is expected to be proportional to that of a self-gravitating disk,

$$\nu_{\rm GD} = G^2\Sigma^2/\Omega^3, \tag{2.9}$$

with a correction factor $C\left(r_{\rm h}\right)$, which depends on the relative importance of inelastic collisions to the self-gravity of a ring. In terms of τ and $r_{\rm h}$, Equation (2.9) can be re-written as (Daisaka et al., 2001)

$$\nu_{\rm GD}/\left(R^2\Omega\right) = (144/\pi^2) r_{\rm h}^6 \tau^2. \tag{2.10}$$

Daisaka et al. (2001) found $C\left(r_h\right) = 26 r_{\rm h}^5$ from a comparison with their numerical results.

Although our results of N-body simulations show that the dependence of the viscosity on optical depth is somewhat stronger than that given by Equation (2.9) (i.e., $d\ln\nu/d\ln\tau > 2$) when viscosity begins to deviate from the $\nu \propto \tau$ relation with increasing τ (Section 2.4), the τ-dependence of our numerical results for the high-τ cases is roughly consistent with Equation (2.9). Therefore, following Daisaka et al. (2001), we evaluate the correction factor $C = \nu/\nu_{\rm GD}$ using our numerical results (Figure 2.9(a)). We find that a correction factor given by

$$C_{\rm wake}\left(r_{\rm h}\right) \simeq 53 r_{\rm h}^5 \tag{2.11}$$

seems to well reproduce our numerical results for dense rings with gravitational wakes (i.e., $r_{\rm h} \sim 0.7$-0.8 and $\tau \gtrsim 0.5$). The fifth-power dependence of the correction factor on $r_{\rm h}$ is consistent with Daisaka et al. (2001), but the numerical coefficient is a factor of about two larger than Daisaka et al. (2001). This is due to the difference in restitution coefficients adopted in these simulations. We used our numerical results for the case with $\varepsilon_{\rm n} = \varepsilon_{\rm n}\left(v\right)$ and $\varepsilon_{\rm t} = 0.5$, while Daisaka et al. (2001) derived their correction factor from their simulations with smooth particles with normal restitution coefficients independent of impact velocity. In fact, we confirmed that our numerical results as well as those obtained by Schmidt et al. (2009) for $\varepsilon_{\rm n} =$

0.5 and $\varepsilon_{\rm t} = 1$ are consistent with Daisaka et al. (2001; Figure 2.9(b)). As we discussed in Section 2.4, including surface friction as well as using the velocity-dependent normal restitution coefficient somewhat increases the viscosity values, which explains the above difference in the correction factor. Thus, it should be noted that our semianalytic expressions shown below include uncertainty of a factor of 2-3 due to uncertainty in elastic properties of ring particles.

Daisaka et al. (2001) argued that the $r_{\rm h}$-dependence of the correction factor is related to "compressibility" of particle disks due to self-gravity. When $r_{\rm h}$ is significantly smaller than unity (e.g. $r_{\rm h} \sim 0.5$), collisions suppress the tendency of formation of gravitational wakes, thus the enhancement of viscosity due to self-gravity is insignificant. This compressibility discussed in Daisaka et al. (2001) can be quantitatively demonstrated by calculating the physical optical depth $\tau_{\rm phys}$ using a spatial distribution of particles obtained by N-body simulation; here, $\tau_{\rm phys}$ is defined so that $\exp(-\tau_{\rm phys})$ is the average fraction of skewers that penetrate the ring without piercing any particles (Figure 2.10; Wisdom & Tremaine, 1988; Robbins et al., 2010). In the case of large τ and $r_{\rm h}$, we confirm significant reduction in $\tau_{\rm phys}$ compared with the dynamical optical depth τ ($= N\pi R^2/L^2$); thus, there is a stronger tendency of particle clumping and wake formation, which results in a significant increase in viscosity.

Figure 2.11(a) shows the plots of our analytic results obtained by $\nu = \max\{\nu_{\rm low}, C_{\rm wake}\nu_{\rm GD}\}$ ($C_{\rm wake}$ is given by Equation (2.11)) together with numerical results of our N-body simulation. We confirm excellent agreement in both low and high optical depth regimes for $r_{\rm h} = 0.5$ - 0.82, as expected. On the other hand, the above analytic expression significantly overestimates the numerical results for $r_{\rm h} = 1$, as can be predicted from the plots of the correction factor in Figure 2.9(a). In the cases of $r_{\rm h} \simeq 1$, the relatively large size of the Hill sphere compared with the particle physical size allows the formation of temporary aggregates rather than gravitational wakes (Salo, 1995), as we mentioned above (Figure 2.8). Therefore, the above disagreement be-

tween the analytic result for the viscosity that is valid in the case of wake formation and the numerical results for $r_{\rm h} \simeq 1$ is not surprising; viscosity in rings with temporary aggregate formation, which likely corresponds to the outer A ring of Saturn, should be treated separately from the case of rings with gravitational wakes. Our numerical results show that the τ^2-dependence suggested by Equation (2.9) also seems to be approximately valid in the case of $r_{\rm h} = 1$ and $\tau \simeq 1$, but the correction factor should be separately determined. Since our numerical results for $r_{\rm h} \simeq 1$ suggest that the dependence of the correction factor on τ is rather weak (Figure 2.9(a)), here we adopt

$$C_{\rm agg} \simeq 30 \tag{2.12}$$

as a simple remedy for the correction factor in the case of temporary aggregate formation. Figure 2.11(b) shows a comparison between the results obtained from the revised semianalytic expression with our results of N-body simulation, where we find excellent agreement for the entire parameter regime examined here.

In summary, our numerical results can be well approximated by the following expression:

$$\nu = \max\left\{\nu_{\rm low}, C\nu_{\rm GD}\right\}, \tag{2.13}$$

where $\nu_{\rm low}$ and $\nu_{\rm GD}$ are given by Equations (2.8) and (2.9), respectively, and the correction factor is $C = \min\{C_{\rm wake}\left(r_{\rm h}\right),\ C_{\rm agg}\}$, where $C_{\rm wake}\left(r_{\rm h}\right)$ and $C_{\rm agg}$ are given by Equations (2.11) and (2.12), respectively. Again, it should be noted that viscosity values obtained by the above expression include an uncertainty factor of about 2-3 due to uncertainty in the elastic properties of particles.

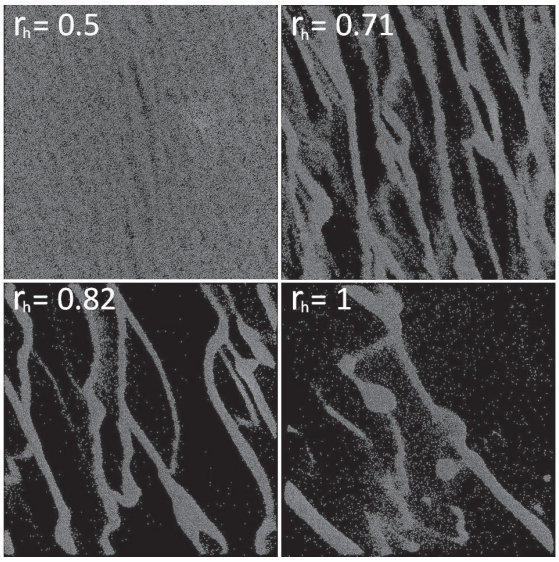

Figure 2.8: Snapshots of the spatial distribution of particles in simulations for four different values of $r_{\rm h}$ in the case of $\tau = 1$ ($\varepsilon_{\rm n} = \varepsilon_{\rm n}(v), \varepsilon_{\rm t} = 0.5$). Particle radius is 1 m, and the size of each panel shown here is about 450 m (from Yasui et al. 2012).

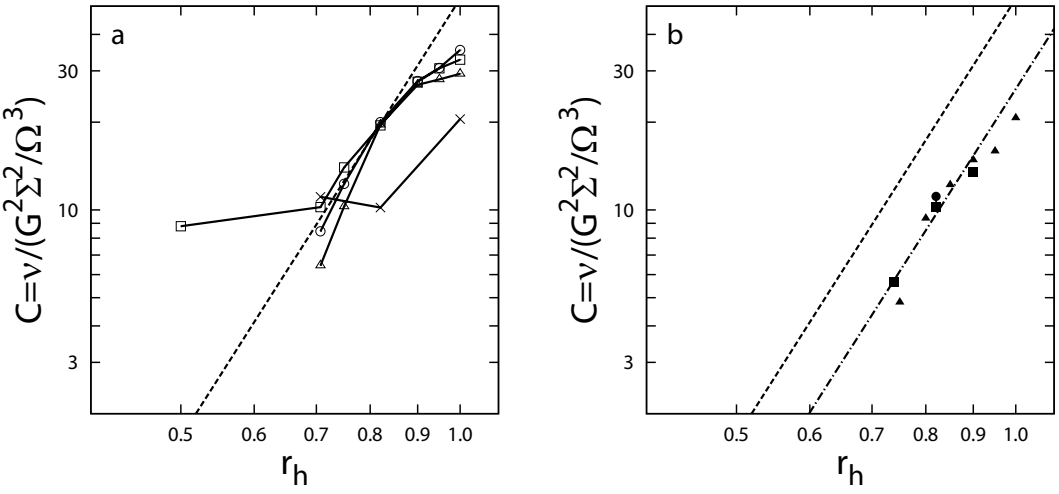

Figure 2.9: Correction factor $C \equiv \nu / \left(G^2\Sigma^2/\Omega^3\right)$ as a function of $r_{\rm h}$. (a) Solid lines with symbols represent the results obtained from our N-body simulations ($\varepsilon_{\rm n} = \varepsilon_{\rm n}(v)$, $\varepsilon_{\rm t} = 0.5$) with τ =0.2 (crosses), 0.5 (triangles), 0.7 (circles), and 1 (squares). Dashed line represents the relation $C_{\rm wake} = 53 r_{\rm h}^5$, which agrees well with our numerical results for the case of the dense rings with gravitational wakes. Note that the tendency to form gravitational wakes is rather weak in the case of $\tau = 0.2$; thus, the values of the correction factor in this case deviate from the line for the semianalytic expression even at $r_{\rm h} = 0.8$-1. (b) Comparison of our numerical result (circle) with the results obtained by Daisaka et al. (2001) (triangles) and Schmidt et al. (2009) (squares) for $\varepsilon_{\rm n} = 0.5$ and $\varepsilon_{\rm t} = 1$ with $\tau = 0.5$. Dashed line is the same as the one shown in (a). Dot-dashed line represents the relation $C = 26 r_{\rm h}^5$ obtained by Daisaka et al. (2001) (from Yasui et al. 2012).

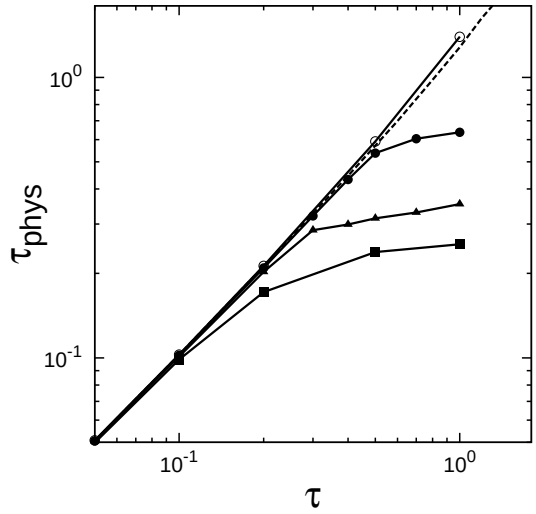

Figure 2.10: Physical optical depth $\tau_{\rm phys}$ as a function of dynamical optical depth $\tau\,(= N\pi R^2/L^2)$. $\tau_{\rm phys}$ is calculated from snapshots of the spatial distribution of particles obtained by our N-body simulation ($\varepsilon_{\rm n} = \varepsilon_{\rm n}\,(v)$, $\varepsilon_{\rm t} = 0.5$). Results for various values of $r_{\rm h}$ are shown; $r_{\rm h}$ =0.5 (open circles), 0.71 (solid circles), 0.82 (triangles), and 1 (squares), respectively. Nongravitating case ($r_{\rm h} = 0$) is also shown by the dashed line (from Yasui et al. 2012).

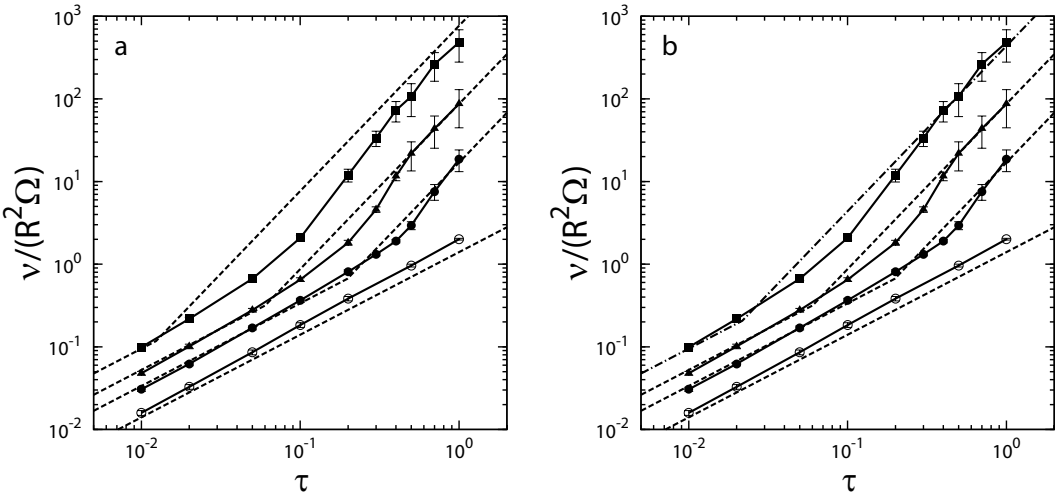

Figure 2.11: (a) Comparison of results obtained by our semianalytic expression (dashed lines) with the numerical results of our N-body simulation (solid lines) for $\varepsilon_{\rm n} = \varepsilon_{\rm n}\,(v)$ and $\varepsilon_{\rm t} = 0.5$. The four lines correspond to the cases with $r_{\rm h}$ =0.5, 0.71, 0.82, and 1, as in Figure 2.7. For the semianalytic results shown here, we used $C_{\rm wake} = 53 r_{\rm h}^5$ given by Equation (2.11) for all the values of $r_{\rm h}$. (b) Same as (a), but $C_{\rm agg} = 30$ is used instead of $C_{\rm wake} = 53 r_{\rm h}^5$ to obtain the semianalytic results for the case with $r_{\rm h} = 1$ (dot-dashed line) (from Yasui et al. 2012).

2.6 Conclusions and Discussion

In the present work, using local N-body simulation, we examined viscosity in self-gravitating rings for a wide range of parameters. We calculated ring viscosity based on the formulation developed by Tanaka et al. (2003), in which viscosity is evaluated by calculating the average energy dissipation rate due to inelastic collisions in N-body simulation. We investigated the dependence of viscosity on various parameters in detail, including the effects of particle surface friction.

In the case of self-gravitating rings with low optical depth, we found that viscosity is determined by particle random velocity, as in the case of nongravitating rings with low optical depth. The effects of surface friction on viscosity were found to depend on the importance of the mutual gravity of the particles relative to collisions, which can be expressed in terms of the ratio of the mutual Hill radius of colliding particles to their physical size ($r_{\rm h}$). When the effects of gravitational encounters are unimportant ($r_{\rm h} \sim 0.5$) and particle random velocity is determined by inelastic collisions, the inclusion of surface friction slightly reduces both random velocity and viscosity. On the other hand, when $r_{\rm h} \sim 1$ and gravitational encounters do play a major role in particle velocity evolution, the inclusion of surface friction results in the increase of viscosity, since the viscous heating increases to balance the increased energy dissipation at collisions due to surface friction. We found that varying restitution coefficients can change the viscosity in dilute rings by a factor of about two.

On the other hand, viscosity is significantly enhanced in dense self-gravitating rings where gravitational wakes are formed (Daisaka et al., 2001). We found that viscosity in dense rings with a given τ and $r_{\rm h}$ is larger when collisions are more dissipative, for example, by the inclusion of surface friction, and the enhancement of viscosity due to this effect can be a factor of about two. Following Daisaka et al. (2001), we assumed that the dependence of viscosity on the optical depth can be approximated by that for a self-gravitating disk (Equation (2.9)), so we evaluated a correction factor using our numerical results of N-body simulation. We found that

the expression for the correction factor of the dense rings with gravitational wakes is similar to the one obtained by Daisaka et al. (2001), the difference of a factor two in the numerical coefficient can be explained by the difference in restitution coefficients that were adopted. On the other hand, in the case of the outer rings where temporary aggregates form due to self-gravity, the above expression overestimates the viscosity values; thus, we derived a revised expression for such a case. We confirmed that the semianalytic expressions we obtained well reproduce our numerical results for the entire range of parameters examined here.

The expression we obtained for the viscosity in the case with low optical depth is consistent with previous theoretical works for nongravitating rings (e.g. Goldreich & Tremaine, 1978). However, the expressions for the viscosity (or the expression for the correction factor) for dense rings were empirically obtained by comparing numerical results. Although the strong $r_{\rm h}$-dependence of the viscosity in the case of the rings with gravitational wakes has been explained by ring compressibility (i.e., the degree of density contrast created as a result of the formation of gravitational wakes), more detailed theoretical modeling of viscosity in self-gravitating collisional disks would be useful for a better understanding of the dynamics in dense planetary rings.

Chapter 3

Gravitational Accretion of Particles onto Moonlets Embedded in Saturn's Rings

3.1 Introduction

Collision and gravitational accretion of particles is an important issue related to the origin of ring-satellite systems of giant planets in the solar system. In contrast to accretion of planetesimals in circumstellar disks, tidal forces cannot be ignored in circumplanetary disks and gravitational accretion of particles is prohibited in the inner part of the disk closer to the central planet. When a small particle and a large one with identical density ρ are in contact and in synchronous rotation with their line of centers pointing to the planet, they become gravitationally bound if they are located outside the critical distance defined as (Weidenschilling et al., 1984)

$$\frac{a}{R_{\rm c}} = 1.44 \left(\frac{\rho_{\rm c}}{\rho} \right)^{1/3}, \tag{3.1}$$

where a is the distance from planet, and $R_{\rm c}$ and $\rho_{\rm c}$ are the mean radius and density of the central planet, respectively. For the case of identical particles, the critical distance is given by

$$\frac{a}{R_{\rm c}} = 2.29 \left(\frac{\rho_{\rm c}}{\rho} \right)^{1/3}. \tag{3.2}$$

On the other hand, a synchronously rotating, self-gravitating liquid satellite cannot maintain hydrostatic equilibrium due to tidal and centrifugal forces within the

classical Roche limit (Chandrasekhar, 1969) given by

$$\frac{a_{\rm R}}{R_{\rm c}} = 2.456 \left(\frac{\rho_{\rm c}}{\rho} \right)^{1/3}. \tag{3.3}$$

Note that Equations (3.1) and (3.2) are similar to Equation (3.3), but the numerical coefficients are different.

Probability of gravitational accretion of colliding ring particles depends on their impact velocity and impact orientation, and are studied using three-body orbital integration (Ohtsuki, 1993; Morishima & Salo, 2004; Ohtsuki et al., 2013). It has been shown that the ratio of the physical size of colliding particles to their mutual Hill radius is an important parameter describing the efficiency of gravitational accretion (Ohtsuki, 1993; Ohtsuki et al., 2013). In rings at a radial distance a from the planet, the ratio of the sum of the physical radii of colliding particles $R_1 + R_2$ to their mutual Hill radius, $R_{\rm H}$ ($= \{(m_1 + m_2)/3M_{\rm c}\}^{1/3} a$), can be written as

$$\tilde{r}_{\rm p} \equiv \frac{R_1 + R_2}{R_{\rm H}} = \left(\frac{9}{4\pi} \right)^{1/3} \rho_{\rm p}^{-1/3} M_{\rm c}^{1/3} a^{-1} \frac{1 + \mu^{1/3}}{(1+\mu)^{1/3}}, \tag{3.4}$$

where $\rho_{\rm p}$ is the density of the particles, $M_{\rm c}$ is the mass of the central planet, m_1 and m_2 are the mass of colliding particles, and μ ($= m_2/m_1$) is their mass ratio ($0 < \mu \leq 1$). Equations (3.1) and (3.2) are equivalent to $\tilde{r}_{\rm p} = 1$ with $R_1 \gg R_2$ and with $R_1 = R_2$, respectively. The semi-axis of the Hill sphere in the azimuthal direction is $(2/3)R_{\rm H}$, while its vertical semi-axis is $c_z R_{\rm H}$ with $c_z = 3^{2/3} - 3^{1/3} \simeq 0.638$ (Appendix C). Ohtsuki (1993) showed that the gravitational capture probability decreases abruptly when $\tilde{r_{\rm p}} \gtrsim 0.7$ because particles overflow their mutual Hill sphere in such a case. Using local N-body simulation, Salo (1992, 1995) and Kaljalainen & Salo (2004) investigated gravitational accretion between particles in Saturn's rings, and showed that aggregates can be formed via gravitational sticking of particles in the outer part of the A ring, if the density of particles is not much smaller than the density of water ice. Furthermore, Kaljalainen (2007) performed simulations of impacts between aggregates in the tidal environment, and showed that outcomes of collisions depend on the distance from Saturn and the mass ratio of colliding

aggregates.

On the other hand, detailed observations of shapes and densities of small ($\lesssim 100$ km mean radius) satellites in Saturn's system have been carried out by the Cassini spacecraft, and the results suggest that these satellites were formed by gravitational accretion (Porco et al., 2007). Aggregates formed by gravitational accretion are expected to shape into the Hill sphere in the region if accretion takes place under strong tidal force, while they take more spherical shapes in regions sufficiently far from the planet (Salo, 1995; Kaljalainen & Salo, 2004). When a satellite or an aggregate entirely fills its Hill sphere, it cannot accrete particles anymore by its gravity alone. In this case, the critical density $\rho_{\rm crit}$ at the distance a is defined as (Porco et al., 2007)

$$\rho_{\rm crit} = \frac{3M_{\rm c}}{\gamma a^3}, \tag{3.5}$$

where γ is a dimensionless shape parameter so that $\gamma a_{\rm sat}^3$ is the volume of the satellite with $a_{\rm sat}$ being the long semi-axis of the satellite ($\gamma = 4\pi/3$ for a spherical satellite with radius $a_{\rm sat}$). In the case of the Hill sphere, we numerically obtain $\gamma \simeq 1.509$ (Leinhardt et al., 2012). The Hill radii of Pan, Daphnis, Atlas, and Prometheus are found to be within 15 % of the observed long axes of these satellites given by the best-fit model ellipsoids. Also, the densities of these satellites ($0.4 - 0.6$ g cm^{-3}) are very low compared to the density of water ice and all approximately equal to the critical density at that distance. From these results, the small satellites within the orbit of Pandora are thought to be formed by accretion of small porous ring particles onto large dense cores, and further accretion seems to have been suppressed when the density of the satellite reaches the critical density at that distance (Porco et al., 2007). Using local N-body simulations, Porco et al. (2007) also demonstrated that a Hill sphere-filling body is produced by accretion of small porous particles onto a large dense core. However, it has not been studied how the degree of particle accretion onto moonlets in the inner parts of Saturn's rings depends on the distance from Saturn.

The shapes of these small ringmoons would also provide clues to the dynamical evolution of Saturn's rings. The fact that the shapes of these ringmoons approximately match those of their associated Hill sphere suggests that the moonlet cores were surrounded by a number of particles when they were formed. On the other hand, Pan and Atlas have the characteristic shapes with equatorial ridges, and are thought to be formed by two stages (Charnoz et al., 2007). First, their precursors whose shapes are similar to their Hill sphere without equatorial ridges were formed when the rings were thick. Then, equatorial ridges were formed through particle accretion onto the equatorial planes of the above formed objects after the rings became sufficiently thin and also before ring particles diffused (Porco et al., 2007; Charnoz et al., 2007). However, effects of dynamical properties of the rings on the shaping of moonlets formed by particle accretion have not been examined in detail.

Sufficiently massive moonlets embedded in rings can alter the structures of the rings. Pan and Daphnis open the Encke and the Keeler gaps in the outer A ring, respectively. Propeller-shaped structures have also been found in Cassini images of Saturn's rings (e.g., Tiscareno et al., 2006, 2008, 2010; Sremčević et al., 2007). These propeller-shaped features are explained by gravitational interaction between ring particles and unseen embedded moonlets. From these observations, the sizes and orbital distributions of these unseen embedded moonlets are obtained, and such information provide us with clues to the evolution of the ring-satellite system. The propeller-shaped structures are mainly observed in the A ring, and the sizes of these embedded moonlets are estimated between tens and thousands of meters. Recently, observations of similar structures have also been reported for the Cassini Division, and the B and C rings (Sremčević et al., 2011; Baillié et al., 2013). From these observations, the existence of a moonlet with size of 1.5 km has been suggested in the B ring, while the existence of boulders with radii $\lesssim$ 10 m and $\lesssim$ 50 m has been inferred for the C ring and the Cassini Division, respectively. Although some of these moonlets either may be collisional shards resulting from the breakup of a

bigger icy progenitor ring body or may have formed by accretion of small low-density ring particles onto larger dense fragments, the origin of these moonlets is not clear. By clarifying the critical radial distance for particle accretion onto moonlets and the dependence of the degree of particle accretion on various parameters (e.g., distance from Saturn, particle density, etc.), we can also give constrains on the origin of these propeller moonlets.

In the present work, we carry out local N-body simulations and study the process of particle accretion onto moonlets in Saturn's rings in detail. We examine the dependence of the degree of particle accretion on the distance from Saturn, and also investigate the effects of dynamical properties of rings on the process of particle accretion. Numerical methods and parameters used in this work are described in Section 3.2. We confirm the validity of our numerical code in Section 3.3. Section 3.4 looks at results of our numerical simulation examples and the dependence of particle accretion on radial distance. In Section 3.5, we examine effects of ring thickness on the process of particle accretion, and Section 3.6 describes effects of other parameters. Our conclusions are presented in Section 3.7.

3.2 Numerical Methods

We perform local N-body simulations, using a code based on our previous works (Daisaka et al., 2001; Yasui et al., 2012). We erect a rotating Cartesian coordinate system with origin at the center of the rectangular simulation cell that moves on a circular orbit with semi-major axis a_0 at the Keplerian angular velocity $\Omega = (GM_c/a_0^3)^{1/2}$ around Saturn. The x-axis points radially outward, the y-axis points in the direction of the orbital motion, and the z-axis is normal to the equatorial plane. As in previous works on propeller structures around moonlets in rings (e.g., Seiß et al. 2005; Sremčević et al. 2007; Lewis & Stewart 2009; Michikoshi & Kokubo 2011) or particle accretion onto moonlets (Porco et al., 2007), a moonlet is set at the origin of the coordinate system (Ohtsuki et al., 2013). Periodic boundary conditions in the radial direction are adopted, taking account of the shear motion of adjacent copied cells (e.g., Wisdom & Tremaine, 1988). However, we do not use the azimuthal periodic boundary conditions so that those particles perturbed by the moonlet do not re-enter the simulation cell through the azimuthal boundaries. Instead, for each time step, particles not yet perturbed by the moonlet are added to the cell from the azimuthal boundaries (Seiß et al. 2005; Sremčević et al. 2007). We assume that particles entering the cell are uniformly distributed in the radial direction. In order to obtain equilibrium velocity in a ring without the moonlet, we perform a separate simulation with periodic boundary conditions without the moonlet. Orbital eccentricities and inclinations of the fresh particles to be added through the azimuthal boundaries are assumed to have Rayleigh distribution (Ohtsuki & Emori, 2000) with r.m.s. values obtained from the above separate simulation. In the simulations presented in Section 3.5, where we examine the effects of ring thickness on particle accretion, eccentricities and inclinations of particles to be added are assumed to have Rayleigh distribution with given r.m.s. values. Particles are removed from the simulation cell when their guiding centers cross the x- or y-axis at least once and then leave the cell through the azimuthal boundaries. On the other hand, particles

can gravitationally accumulate on the moonlet's surface. Thus, the number of particles in the cell is not constant in our simulations. We take the size of the simulation cell to be large enough to neglect effects of the boundaries on the process of particle accretion onto the moonlet (typically, $\sim 30R_{\rm H,m}$ and $\sim 80R_{\rm H,m}$ in the azimuthal and radial directions, respectively, where $R_{\rm H,m}$ is the moonlet's Hill radius).

The equations of motion of particle i are written as

$$\begin{aligned}
\ddot{x}_i &= 2\dot{y}_i\Omega + 3x_i\Omega^2 - \frac{Gm_{\rm m}\left(x_i - x_{\rm m}\right)}{r_{i{\rm m}}^3} - \sum_{j\neq i}^{N}\frac{Gm_j\left(x_i - x_j\right)}{r_{ij}^3} \\
\ddot{y}_i &= -2\dot{x}_i\Omega - \frac{Gm_{\rm m}\left(y_i - y_{\rm m}\right)}{r_{i{\rm m}}^3} - \sum_{j\neq i}^{N}\frac{Gm_j\left(y_i - y_j\right)}{r_{ij}^3} \\
\ddot{z}_i &= -z_i\Omega^2 - \frac{Gm_{\rm m}\left(z_i - z_{\rm m}\right)}{r_{i{\rm m}}^3} - \sum_{j\neq i}^{N}\frac{Gm_j\left(z_i - z_j\right)}{r_{ij}^3},
\end{aligned} \tag{3.6}$$

where $\boldsymbol{x}_i = (x_i,\ y_i,\ z_i)$ and $\boldsymbol{x}_{\rm m} = (x_{\rm m},\ y_{\rm m},\ z_{\rm m})$ are the coordinates of the particle and the moonlet, respectively, $r_{i{\rm m}} = [(x_i - x_m)^2 + (y_i - y_m)^2 + (z_i - z_m)^2]^{1/2}$, $r_{ij} = [(x_i - x_j)^2 + (y_i - y_j)^2 + (z_i - z_j)^2]^{1/2}$, $m_{\rm m}$ is the mass of moonlet, $m_{\rm j}$ is the mass of particle j, and N is the particle number. The moonlet is initially placed at the origin at rest in the rotating coordinate system. However, particles hit the moonlet and some of them accumulate on it. Especially, in the case of simulations for the outer part of Saturn's main rings, many particles accrete onto the moonlet, and mass shedding from the aggregate occurs in the sub- and anti-Saturn directions asymmetrically (Section 3.4). This changes the moonlet's orbital angular momentum significantly and causes its radial drift (Lewis & Stewart, 2009). In order to simulate such behavior accurately, we also integrate the equations for the motion of the moonlet in simulations for the outer rings. In such a case, in order to keep the moonlet near the center of the simulation cell, we carry out coordinate transformation each time step so that the guiding center of the moonlet always stays at the center of the cell. Motion of the moonlet is also integrated for the cases with particle size distribution (Section 3.6.2), because the assumed mass of the largest ring particles is not negligible compared to the mass of the moonlet ($m_{\rm p,max}/m_{\rm m} = 0.064$ in our

simulations with particle size distribution, where $m_{\rm p,max}$ is the mass of the largest ring particles). On the other hand, in the cases of simulations with identical ring particles and in inner parts of Saturn's main rings (from the C ring to the Cassini Division), the assumed mass of particles is small enough compared to the mass of moonlet ($m_{\rm p}/m_{\rm m} \leq 3.375 \times 10^{-3}$, where $m_{\rm p}$ is the mass of particles), and also the total mass of particles that accrete onto the moonlet is much smaller than the moonlet mass. In this case, particles accrete onto the moonlet on the sub- and anti-Saturn sides almost symmetrically, and the net angular momentum given to the moonlet during mass shedding is very small. For these reasons, the moonlet is fixed at the origin of the simulation cell in simulations for such cases. We confirmed the validity of this assumption by comparing with results of simulations that allow the moonlet's motion. Gravitational forces are directly calculated using GRAPE-7 or GRAPE-9, which is a special-purpose hardware for calculating gravitational forces, and orbits are integrated with the second-order leap-frog method. When moonlet-particle or particle-particle collisions are detected, velocity changes are calculated based on the hard-sphere model with the normal restitution coefficient $\varepsilon_{\rm n}$ given as a parameter, assuming that moonlet and particles are smooth spheres. In the cases of dilute rings, $N \sim 10^3$ is used in our simulations, while we use $10^4 - 10^5$ particles in the cases of dense rings ($\tau \geq 0.1$) or rings with particle size distribution.

The criteria for gravitational accretion of colliding two bodies was derived based on the Hill approximation in the three-body problem (Ohtsuki, 1993). The criteria state that they can become gravitationally bound if they are within their mutual Hill radius and $E < 0$ after inelastic collisions, where E is the sum of the relative kinetic energy and tidal potential energy of colliding particles. However, when particles accrete on a moonlet to form an aggregate, the above criteria cannot be used for the gravitational accretion of particles by the moonlet, because the effect of the self-gravity of the particles accreted onto the moonlet becomes significant but is not taken into account in the above criteria. Therefore, as an alternative criterion, we regard a

particle as a member of the aggregate if it is in contact with the aggregate including the moonlet. Using this criterion, we examine evolution of the mass of aggregates.

Following three factors are important in particle accretion onto moonlets: size of the moonlet's Hill sphere, the ratio of the particle's physical size to that of the moonlet, and the self-gravity of particles accreted onto the moonlet. In this work, we use the following three non-dimensional parameters describing the importance of the above factors:

$$\tilde{r}_{\rm h,m} \equiv R_{\rm H,m}/R_{\rm m}, \quad \tilde{r} \equiv R_{\rm p}/R_{\rm m}, \quad \tilde{\rho} \equiv \rho_{\rm p}/\rho_{\rm m}. \tag{3.7}$$

In the above R and ρ are the radius and the density, with subscripts m and p representing moonlet and particle, respectively, and $R_{\rm H,m} = a\left(m_{\rm m}/\left(3M_{\rm c}\right)\right)^{1/3}$ is the Hill radius of the moonlet. Figure 3.1 shows the plots of $\tilde{r}_{\rm h,m}$ as a function of the distance from Saturn for several values of $\rho_{\rm m}$. The moonlet's Hill sphere covers the entire surface of the moonlet for $\tilde{r}_{\rm h,m} \geq c_z^{-1} \simeq 1.57$ (Figure 3.1). In our simulations with identical particles, we use $\tilde{r} = 0.05$ and 0.15 in the cases of $\tilde{r}_{\rm h,m} < c_z^{-1}$ and $\tilde{r}_{\rm h,m} \geq c_z^{-1}$, respectively. We confirmed the dependence of the final mass of aggregates on $\tilde{r}$ is negligible as long as we use such small values of $\tilde{r}$. On the other hand, $R_{\rm p,max}/R_{\rm m} = 0.4$ is used in cases with particle size distribution following Porco et al. (2007), where $R_{\rm p,max}$ is the radius of the largest particle. In order to study effects of ring thickness on particle accretion, we also define the ring thickness normalized by the moonlet's radius;

$$\tilde{h} \equiv a\langle i_{\rm p}^2\rangle^{1/2}/R_{\rm m}, \tag{3.8}$$

where $i_{\rm p}$ is the orbital inclination of the particles. Furthermore, we give the dynamical optical depth τ ($= N\pi R_{\rm p}^2/L_xL_y$, where L_x and L_y are the radial and azimuthal lengths of the simulation cell) and the normal restitution coefficient $\varepsilon_{\rm n}$ as parameters, and also examine the effects of these parameters on particle accretion. We assume uniform particle sizes in Sections 3.4, 3.5 and 3.6.1, and particle size distribution is taken into account in Section 3.6.2. The list of the above parameters and their

definitions are summarized in Table 3.1.

Table 3.1: Definition of symbols used in the present paper

Symbol	definition	meaning
$\tilde{r}_{\rm h,m}$	$R_{\rm H,m}/R_{\rm m}$	Hill radius of the moonlet relative to its physical radius
$\tilde{r}$	$R_{\rm p}/R_{\rm m}$	Size of a ring particle relative to the moonlet
$\tilde{\rho}$	$\rho_{\rm p}/\rho_{\rm m}$	Internal density of ring particles relative to the moonlet
$\tilde{h}$	$\langle i_{\rm p}^2\rangle^{1/2} a/R_{\rm m}$	Vertical thickness of the ring relative to the moonlet radius

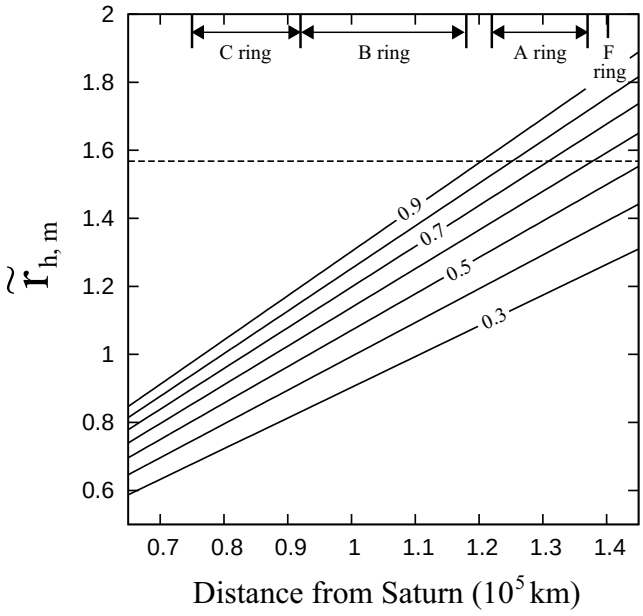

Figure 3.1: Dependence of $\tilde{r}_{\rm h,m}$ on the radial distance from Saturn for several values of moonlet internal density. Cases for $\rho_{\rm m} = 0.3 - 0.9$ g cm^{-3} are shown with an interval of 0.1 g cm^{-3}. Dashed line represents $\tilde{r}_{\rm h,m} = c_z^{-1} \simeq 1.57$ (from Yasui et al. 2014).

3.3 Test Simulation: Comparison with Three-Body Calculations

Here, we perform N-body simulations of accretion of small ring particles by an embedded moonlet, and compare collision and accretion rates with those obtained by the three-body calculations obtained by Ohtsuki et al. (2013) in order to confirm the validity of our N-body code.

The rates of collision and gravitational capture are defined as follows. We use scaled orbital elements $\tilde{e}$, $\tilde{i}$, $\tilde{b}$, where $\tilde{e}$ and $\tilde{i}$ are the eccentricity and inclination for the relative motion scaled by $h \equiv [(m_{\rm p}+m_{\rm m})/(3M_{\rm c})]^{1/3}$, and $\tilde{b} \equiv (a_2-a_1)/R_{\rm H}$ is the difference in semimajor axes of the moonlet and a particle scaled by their mutual Hill radius. For each orbit with initial orbital elements $\tilde{e}$, $\tilde{i}$, $\tilde{b}$, τ, and ϖ (τ and ϖ are horizontal and vertical orbital phases for the relative motion, respectively), we define $p_{\rm col}$ as $p_{\rm col}=1$ for collision orbits and zero otherwise. Similarly, we define $p_{\rm cap}$ as $p_{\rm cap}=1$ for collision orbits that lead to accretion after impact(s), and zero otherwise. Using $p_{\rm col}$, the collision rate per unit surface number density of particles is defined as (Nakazawa et al. 1989)

$$P_{\rm col}(\tilde{e},\tilde{i}) \equiv \int p_{\rm col}(\tilde{e},\tilde{i},\tilde{b},\tau_{\rm oe},\varpi)\frac{3}{2}|\tilde{b}|d\tilde{b}\frac{d\tau d\varpi}{(2\pi)^2}. \tag{3.9}$$

The rate of gravitational capture within the Hill sphere can be defined similarly as (Ohtsuki 1993)

$$P_{\rm cap}(\tilde{e},\tilde{i}) \equiv \int p_{\rm cap}(\tilde{e},\tilde{i},\tilde{b},\tau_{\rm oe},\varpi)\frac{3}{2}|\tilde{b}|d\tilde{b}\frac{d\tau d\varpi}{(2\pi)^2}. \tag{3.10}$$

Then, the probability of gravitational capture for colliding particles with a given pair of $\tilde{e}$ and $\tilde{i}$ can be defined as $C(\tilde{e},\tilde{i}) = P_{\rm cap}(\tilde{e},\tilde{i})/P_{\rm col}(\tilde{e},\tilde{i})$ (Ohtsuki 1993).

Using the non-dimensional collision rate, the number of particles that undergo their first impact onto the moonlet per unit time can be written as $N_{\rm s}R_{\rm H}^2\langle P_{\rm col}\rangle\Omega$, where $N_{\rm s}$ is the surface number density of the small particles. The number of such collisions in one orbital period can be written as $N_{\rm col} \equiv 2\tau\langle P_{\rm col}\rangle R_{\rm H}^2/R_{\rm p}^2$. In order to facilitate comparison between numerical results for different values of τ, we define

$N^*_{\rm col} \equiv N_{\rm col}/\tau$, which we call the normalized collision rate. Similarly, we define the normalized accretion rate $N^*_{\rm cap} \equiv N_{\rm cap}/\tau$, where $N_{\rm cap} \equiv 2\tau\langle P_{\rm cap}\rangle R_{\rm H}^2/R_{\rm p}^2$ is the number of particles gravitationally captured by the moonlet in one orbital period.

First, we compare results of N-body simulations with three-body results, neglecting the effect of aggregate formation. A 20m-radius moonlet is embedded in a low-optical-depth swarm ($\tau = 10^{-3}$ or 10^{-2}) of 1m-radius particles orbiting about a Saturn-mass central planet. Their densities are assumed to be 0.9 g cm^{-3}, and two cases of different radial locations are considered, i.e., $a = 8.06\times10^9$ cm and 1.15×10^{10} cm, so that the value of $\tilde{r}_{\rm p}$ for each case is 1 and 0.7, respectively; gravitational accretion is prohibited in the former case. In the first set of simulations, in order to neglect the effect of aggregate formation, particles that become gravitationally bound to the moonlet (i.e., those have negative energy after impact(s) with the moonlet) are removed from the system. With this treatment, $\tilde{r}_{\rm p}$ for moonlet-particle collisions is kept constant. Also, in order to be consistent with the definition of the collision rate given by Equation (3.9), only each particle's first impact onto the moonlet is counted in the calculation of $N^*_{\rm col}$. Smooth particles are used in the N-body simulation while three-body results for the case with weak friction are used for the comparison, but this effect is negligible (Ohtsuki et al. 2013).

Figure 3.2 shows the plots of the normalized collision and accretion rates defined above, as a function of the normalized time ($t\tau$). The three horizontal dotted lines represent the collision and accretion rates calculated from the three-body results. The top horizontal line represents the collision rate in the case of $\tilde{r}_{\rm p} = 0.7$; the middle one represents the accretion rate also for $\tilde{r}_{\rm p} = 0.7$; and the bottom one represents the collision rate in the case of $\tilde{r}_{\rm p} = 1$. These are calculated using the three-body results of the collision and accretion rates with the value of the unperturbed steady-state velocity dispersion and the given value of $\tilde{r}_{\rm p}$. The solid lines with marks and error bars represent the results of N-body simulation for dilute rings ($\tau = 10^{-3}$ or 10^{-2}). These results show that collision and accretion rates in optically thin rings can be

well approximated by the results of three-body orbital integration when the effect of aggregate formation can be neglected and the assumption of a constant $\tilde{r}_{\rm p}$ is valid.

Next, we examine the effect of aggregate formation. We consider the case with the same parameter values as in the $\tilde{r}_{\rm p} = 0.7$ case in Figure 3.2. In this simulation, we do not remove those particles which become gravitationally bound to the moonlet. Figure 3.3(a) shows the plots of the normalized accretion rate in this case, as a function of the normalized time. At the initial stage of accretion, the surface of the moonlet is not covered by particles, and the particles can collide directly onto the surface of the moonlet. As a result, the accretion rate calculated from the results of N-body simulation agrees with the three-body results very well. As accretion of particles proceeds and they gradually fill the remaining space within the moonlet's Hill sphere (at the normalized time $\sim 0.1 - 0.3$), accretion rates calculated from the N-body results slightly increase, because those particles accreted onto the moonlet effectively increase the collision cross section of the moonlet. Then, the accretion rate is significantly reduced as compared to the three-body results. After that, the accretion rates show both positive and negative values; negative values take place when the number of particles that form the aggregate is decreased compared to the number at the previous sampling time, and the change of the particle number reaches a quasi-steady state (Figure 3.3(b)). Figure 3.4 is a snapshot of the simulation at this stage. We can see that the shape of the aggregate is similar to that of the Hill sphere, as demonstrated by previous studies of accretion in the Roche zone (Salo 1995; Karjalainen & Salo 2004; Porco et al. 2007). We will describe our numerical results in more detail in Sections 3.4 to 3.6.

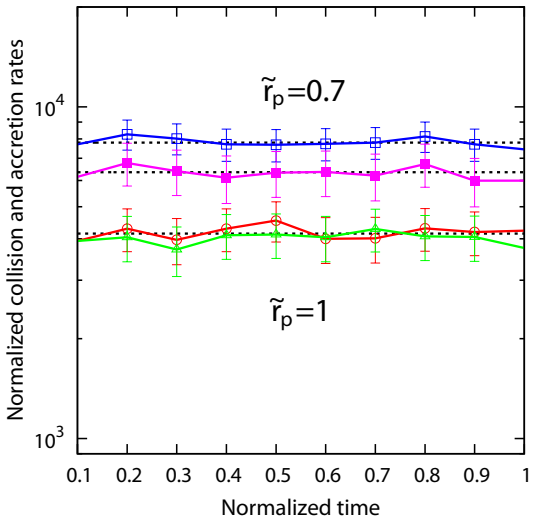

Figure 3.2: Normalized collision rate ($N^*_{\rm col}$) and accretion rate ($N^*_{\rm cap}$) as a function of the normalized time ($t\tau$), in the case where the effect of aggregate formation is neglected (see text). Thin horizontal dotted lines represent the results obtained from the three-body calculations: collision rate for $\tilde{r}_{\rm p} = 0.7$ (top), accretion rate for $\tilde{r}_{\rm p} = 0.7$ (middle), and collision rate for $\tilde{r}_{\rm p} = 1$ (bottom). Solid lines with marks and error bars represent the results of N-body simulation: lines with open squares (colored blue) and filled squares (colored magenta) represent collision and capture rates, respectively, for $\tilde{r}_{\rm p} = 0.7$ and $\tau = 10^{-2}$; and ines with circles (colored red) and triangles (colored green) represent collision rates for $\tau = 10^{-3}$ and 10^{-2}, respectively, with $\tilde{r}_{\rm p} = 1$ ($\varepsilon_{\rm n} = 0.5$) (from Ohtsuki, Yasui, & Daisaka 2013).

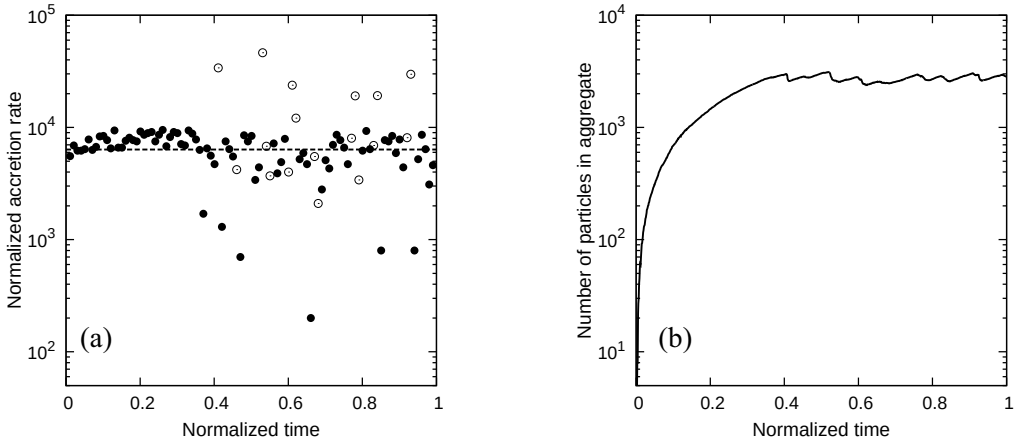

Figure 3.3: Numerical results of N-body simulation for the case with the effect of aggregate formation ($\tilde{r}_{\rm p} = 0.7$, $\varepsilon_{\rm n} = 0.5$, $\tau = 10^{-2}$). (a) Normalized accretion rates as a function of the normalized time. The horizontal dotted line represents the results based on the three-body calculations, while the circles represent the results of N-body simulation. Open circles represent negative values of the accretion rate. (b) Number of particles contained in the aggregate formed on top of the moonlet, as a function of the normalized time (from Ohtsuki, Yasui, & Daisaka 2013).

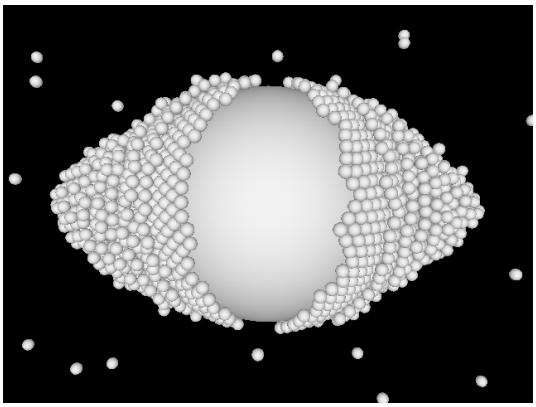

Figure 3.4: Snapshot of the N-body simulation shown in Figure 3.3, at the normalized time 0.45. In this simulation, a 20m-radius moonlet is embedded in a swarm of 1m-radius ring particles, and the radial location from the central planet corresponds to $\tilde{r}_{\rm p} = 0.7$ for moonlet-particle collisions ($\varepsilon_{\rm n} = 0.5$, $\tau = 10^{-2}$) (from Ohtsuki, Yasui, & Daisaka 2013).

3.4 Numerical Results: Degree of Particle Accretion

As we have mentioned above, the entire surface of the moonlet is within its Hill sphere when $\tilde{r}_{\rm h,m} \geq c_z^{-1} \simeq 1.57$, while part of its surface overflows the Hill sphere when $\tilde{r}_{\rm h,m} < c_z^{-1}$. In this section, we first present numerical results for typical cases of partial coverage ($\tilde{r}_{\rm h,m} = 1.5$; Section 3.4.1) and complete coverage ($\tilde{r}_{\rm h,m} = 1.69$; Section 3.4.2) of moonlet surface by particles, as examples of our numerical simulations. When $\rho_{\rm m} = 0.9$ g cm^{-3}, $\tilde{r}_{\rm h,m} = 1.5$ and 1.69 correspond to $a/10^5$ km $= 1.15$ and 1.3 in the Saturnian system, respectively. However, if $\rho_{\rm m} = 0.4$ g cm^{-3}, the above two values of $\tilde{r}_{\rm h,m}$ correspond to $a/10^5$ km $= 1.4$ and 1.58, respectively. In Section 3.4.3, we describe the dependence of particle accretion on radial distance from Saturn.

3.4.1 Case of Partial Coverage of Moonlet Surface

The solid line in Figure 3.5 shows the mass of the aggregate formed around the moonlet as a function of time in the case of $\tilde{r}_{\rm h,m} = 1.5$. The aggregate mass $m_{\rm agg}$ includes both the moonlet and particles accreted, thus the surface of the moonlet is not covered by any particles when $m_{\rm agg}/m_{\rm m} = 1$. Accretion of particles onto the moonlet proceeds at nearly constant accretion rate until $t \simeq 40T_{\rm K}$, because the surface of the moonlet is not yet covered by particles significantly at this stage and the accretion rate is determined by two-body collision between the moonlet and individual particles (Ohtsuki et al., 2013). At $t \simeq 40T_{\rm K}$, accreted particles nearly fill the moonlet's Hill sphere and the aggregate mass reaches an equilibrium value of $m_{\rm agg}/m_{\rm m} \simeq 1.3 - 1.4$. Then, shedding of particles occurs from the vicinity of the L_1 and L_2 Lagrange points of the aggregate (Lewis & Stewart, 2009) and, after that, the aggregate repeats accretion and shedding of particles.

Figure 3.6 shows snapshots of the aggregate at different times. From Figure 3.6(c), one can see that the aggregate is shedding a number of particles from the sub-Saturn side of the aggregate, while releasing of a small number of particles is also taking place at the opposite side. In the quasi-steady state, the aggregate repeats the states (b) to

(d). The amount of shed particles is different at each event and their fraction to the total mass of accreted particles in the aggregate just before the event is about $1-10$ %. The mass shedding does not occur at both sides simultaneously but takes place at each side at different times. Figure 3.7(a) shows the snapshot of the aggregate in the quasi-steady state. One can see that the shape of the aggregate extends in the radial direction due to the effect of mutual gravity between accreted particles, and particles cover the moonlet surface only partially.

Particles accreting on the moonlet surface form layered structure, and clarification of the accretion process would be important for the understanding of the origin of the ringmoons. We examined the accretion process of individual particles onto the moonlet by detailed analysis of snapshots. The first stage of particle accretion is the formation of the bottom layer, mainly by the following three mechanisms. (1a) Particles become gravitationally bound to the moonlet through energy dissipation at direct collision with the moonlet, (1b) energy dissipation at collision on the moonlet surface with other particles already accreted, and (1c) particles hit the first layer and start rolling over it, and then fall to the moonlet surface to be added to the edge of the first layer. We found that the first layer is formed mainly by the mechanisms (1a) and (1b). While the bottom layer is still forming, the second layer begins to form. There are four mechanisms for forming the second layer. (2a) Particles accrete on top of the first layer directly, (2b) particles bounce on the moonlet surface and land on top of the first layer to form the second layer, (2c) particles forming the edge of the first layer are raised to the second layer by oblique impacts of other particles, and (2d) particles forming upper layer(s) roll and fall to be added to the edge of the second layer (similar to (1c)). The second layer is formed mainly by the mechanisms (2a) and (2b). Similarly, while the second layer is still forming, the third layer begins to form. Although mechanisms for forming the third layer are almost the same, it is also formed by particles that bounce on the first layer and then accrete on top of the second layer. Upper layers continue forming through processes similar to (2a), (2c)

and (2d), mainly through (2a).

Although the thickness of the ring in the present case is one-tenth of the moonlet's radius ($\tilde{h} = 0.1$), Figure 3.7(a) shows that particles accrete onto the region of high latitude on the moonlet surface. From detailed analysis of snapshots, we found that mechanisms for placing particles to high latitudes depend on whether the bottom layer is already formed. When the bottom layer is not developed significantly, the dominant mechanism for placing particles to high latitudes is collision between unbound particles on the moonlet surface. Such collisions can place particles that were originally in the region of low latitude on the moonlet surface to high latitudes. When the formation of the bottom layer proceeds, collisions that involve already bound particles at the edge of the first layer often result in placing one of colliding particles to high latitudes. Because the ring thickness is small compared to the moonlet radius in the present case, direct accretion onto the region of the high latitudes did not occur. Effects of ring thickness will be discussed in detail in Section 3.5.

We also examine cases with various values of $\varepsilon_{\rm n}$. The accretion rate of particles in the initial phase of aggregate growth increases with decreasing $\varepsilon_{\rm n}$, because the larger energy dissipation facilitates particle accretion (Ohtsuki, 1993; Ohtsuki et al., 2013). However, differences in the equilibrium aggregate mass and subsequent evolution were found to be negligible. The dependence of the aggregate's shape on $\varepsilon_{\rm n}$ was also found to be rather weak. Particle accretion is somewhat enhanced near the equator of the moonlet when $\varepsilon_{\rm n}$ is small, but the difference was rather small.

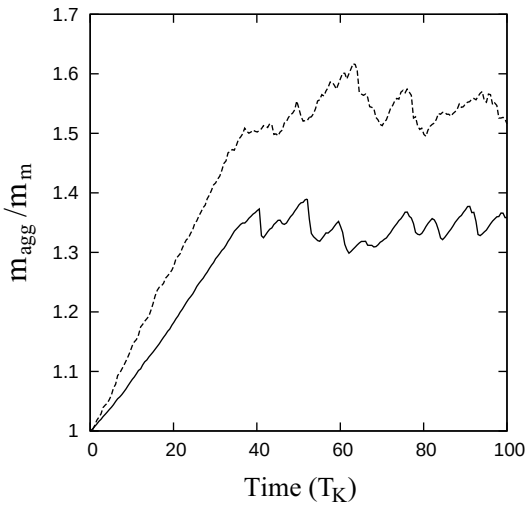

Figure 3.5: Evolution of the mass of the aggregate (i.e, moonlet plus particles accreted onto it) normalized by the moonlet mass ($T_{\rm K} = 2\pi/\Omega$ is the orbital period). The solid and dashed lines show the results for $\tilde{r}_{\rm h,m} = 1.5$ ($\tilde{r} = 0.05,\ \tilde{\rho} = 1$) and $\tilde{r}_{\rm h,m} = 1.69$ ($\tilde{r} = 0.13,\ \tilde{\rho} = 0.44$), respectively. We assumed $\tau = 0.01$, $\varepsilon_{\rm n} = 0.5$, and $\tilde{h} = 0.1 - 0.2$ in these cases (from Yasui et al. 2014).

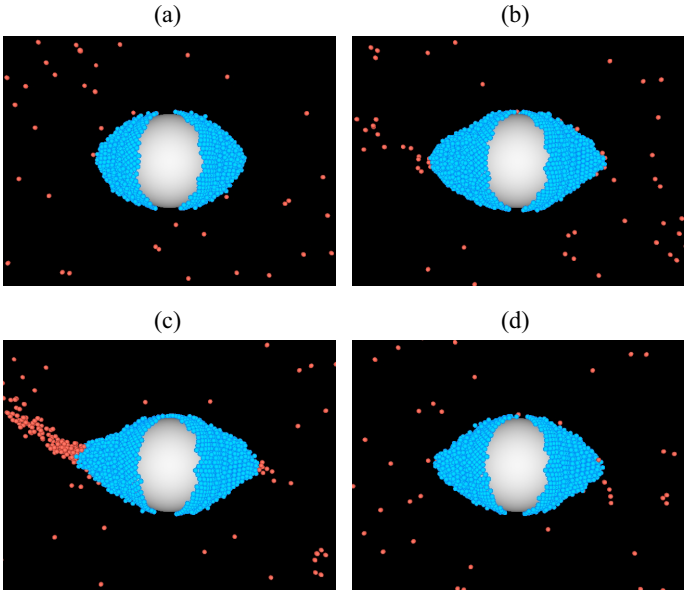

Figure 3.6: Snapshots of particle distribution around the moonlet for four different times in the case of $\tilde{r}_{\rm h,m} = 1.5$ ($\tilde{r} = 0.05$, $\tilde{\rho} = 1$, $\tilde{h} = 0.1$, $\tau = 0.01$, $\varepsilon_{\rm n} = 0.5$). A large white object is the moonlet. Blue particles are those regarded as members of the aggregate, while red ones are not. Panels (a), (b), (c), and (d) are the snapshots at $t \simeq 30$, 51, 53, and 55 $T_{\rm K}$, respectively (from Yasui et al. 2014).

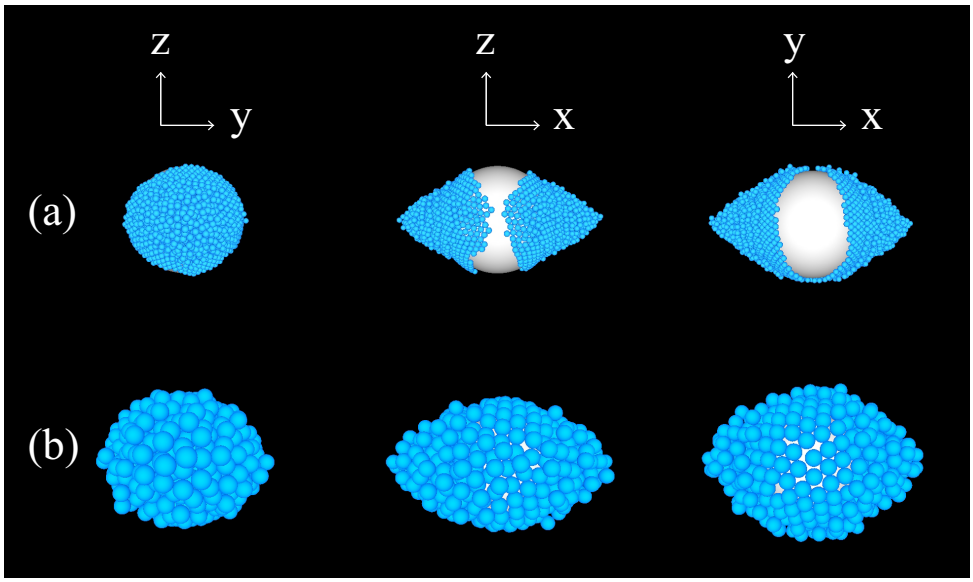

Figure 3.7: Snapshots of the distribution of particles accreted on the moonlet in the quasi-steady state, viewed from three directions as shown on the top of the figure. Panel (a) shows the case with $\tilde{r}_{\rm h,m} = 1.5$, $\tilde{r} = 0.05$, and $\tilde{\rho} = 1$, while Panel (b) shows the case with $\tilde{r}_{\rm h,m} = 1.69$, $\tilde{r} = 0.13$, and $\tilde{\rho} = 0.44$. A large white object is the moonlet and blue particles are those regarded as members of the aggregate. We assumed $\tau = 0.01$, $\varepsilon_{\rm n} = 0.5$, and $\tilde{h} = 0.1 - 0.2$ in these cases (from Yasui et al. 2014).

3.4.2 Case of Complete Coverage of Moonlet Surface

Next, we examine the case with $\tilde{r}_{\rm h,m} = 1.69$, where the moonlet surface is completely covered by its Hill sphere. The dashed line in Figure 3.5 represents the growth of the aggregate mass in this case. After the quasi-steady state is achieved, the aggregate repeats accretion and shedding of particles, as in the case of $\tilde{r}_{\rm h,m} = 1.5$. Also, as in the previous case, particles are released from the vicinity of the Lagrangian points of the aggregate. The equilibrium mass of the aggregate in the present case is larger and is about $1.5 - 1.6$ times the moonlet mass.

Figure 3.7(b) shows the shape of the aggregate in the quasi-steady state for the present case, where we find that particles cover the entire surface of the moonlet. Although the thickness of the ring is much smaller than the radius of the moonlet, particles completely cover the top and bottom of the moonlet. In the present case, in the early stage of accretion, particles accrete to high latitudes of the moonlet surface

by the same mechanisms as in the case of $\tilde{r}_{\rm h,m} = 1.5$. However, when particles completely cover the equator of the moonlet, a different mechanism becomes important. At such a stage, particles colliding on top of the bottom layer slip into the layer by themselves or aided by further collisions with other particles, shoving the edge of the layer towards the region of high latitude. In this way, particles can accrete to high latitudes of the moonlet surface, even though the thickness of the ring is much smaller than the radius of the moonlet.

3.4.3 Dependence of Degree of Particle Accretion on Radial Distance

Next, we investigate how the degree of particle accretion depends on the distance from Saturn. Here we calculate the equilibrium value of the aggregate mass from its time average after the aggregate reaches the quasi-steady state. Figure 3.8 shows the equilibrium mass of aggregates as a function of the distance from Saturn. The vertical dotted line represents the semi-major axis corresponding to $\tilde{r}_{\rm h,m} = c_z^{-1} \simeq 1.57$ assuming $\rho_{\rm m} = 0.9$ g cm^{-3}. When the density of the moonlet is given by this value, accretion of particles over the entire surface of the moonlet is possible beyond this critical semi-major axis. Assuming that the final shape of the aggregate becomes its Hill sphere, Porco et al. (2007) derived an analytic expression for the final semi-axis $R_{\rm agg}$ of the aggregate formed in such an outer region as

$$\frac{R_{\rm agg}}{R_{\rm m}} = \left(\frac{4\pi}{3\gamma} \times \frac{\rho_{\rm m} - \rho_{\rm mantle}}{\rho_{\rm crit} - \rho_{\rm mantle}} \right)^{1/3}, \tag{3.11}$$

where $\rho_{\rm mantle}$ is the bulk density of the mantle of the aggregate, which is given by the internal density of the particles times their filling factor in the mantle, and $\rho_{\rm crit}$ is given by Equation (3.5). Note that the above expression is valid only for $\rho_{\rm crit} > \rho_{\rm mantle}$. From Equation (3.11), the final mass of aggregates can be obtained as

$$\frac{m_{\rm agg}}{m_{\rm m}} = \frac{\rho_{\rm crit}}{\rho_{\rm m}} \times \frac{\rho_{\rm m} - \rho_{\rm mantle}}{\rho_{\rm crit} - \rho_{\rm mantle}}. \tag{3.12}$$

The dashed line in Figure 3.8 is drawn for the outer region using Equation (3.12) for $\rho_{\rm mantle} = 0.28$ g cm^{-3}, where we assumed that $\rho_{\rm p} = 0.4$ g cm^{-3} and the filling

factor is 0.7. We confirm that our numerical results are consistent with the analytic expression given by Equation (3.12).

In the region with $\tilde{r}_{\rm h,m} < 1.57$, where particles can accrete the surface of the moonlet partially, the degree of particle accretion decreases and the mass of the aggregate approaches that of the moonlet with decreasing radial distance. When $\rho_{\rm p} = 0.4$ g cm^{-3}, particle accretion onto a moonlet with $\rho_{\rm m} = 0.9$ g cm^{-3} becomes negligible at the inner B ring (open circles). If particles' internal density is as high as that of water ice ($\rho_{\rm p} = 0.9$ g cm^{-3}), the increased effect of self-gravity of accreted particles facilitates particle accretion (solid marks), and the critical distance for particle accretion becomes near the outer edge of the C ring. However, comparison between photometric modeling and observations of brightness asymmetry in the A ring (Salo et al., 2004) as well as observations of the densities of small ringmoons (Porco et al., 2007) suggest that ring particles are rather underdense, thus the above high density for ring particles seems unlikely. We will further examine effects of particle density in Section 3.6.1. We find that the degree of mass increase of the moonlet by particle accretion (i.e., $m_{\rm agg}/m_{\rm m}$) in the region between the B ring and the Cassini Division is $1 - 1.5$ and $1 - 1.3$ for the cases of $\rho_{\rm p} = 0.9$ g cm^{-3} and 0.4 g cm^{-3}, respectively (Figure 3.8). In the mid-A ring, it is ~ 3 and ~ 1.5 for the cases of $\rho_{\rm p} = 0.9$ g cm^{-3} and 0.4 g cm^{-3}, respectively (Figure 3.8).

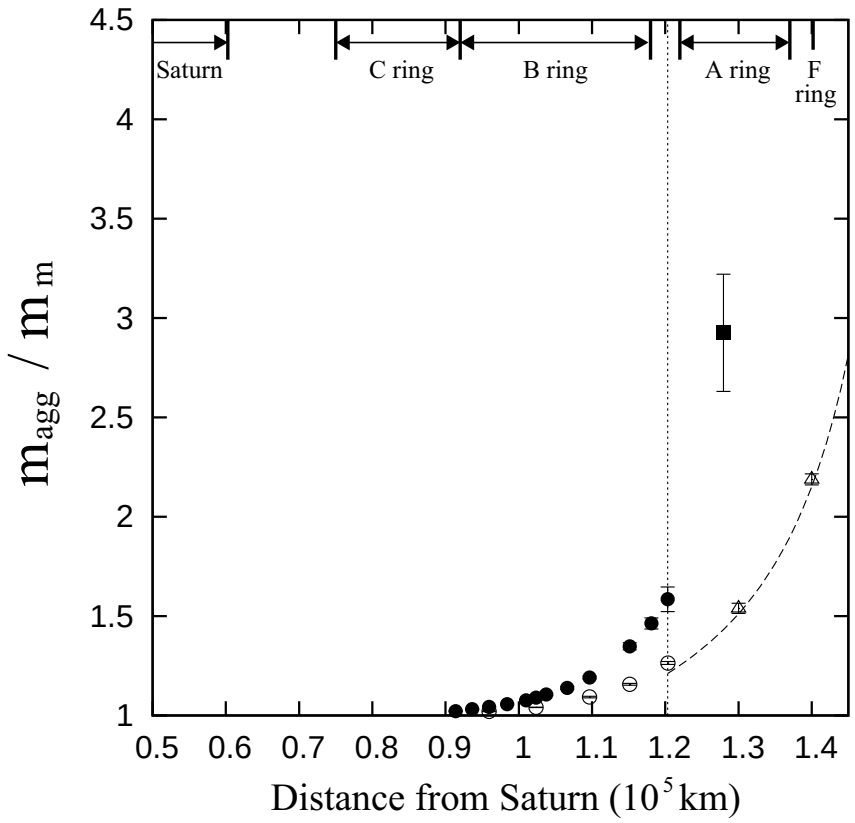

Figure 3.8: Dependence of equilibrium mass of aggregate on the radial distance from Saturn. Circles, triangles, and the square represent results with $\tilde{r} = 0.05$, 0.13, and 0.15, respectively. Open and solid symbols show the results with $\rho_{\rm p} = 0.4$ g cm^{-3} and 0.9 g cm^{-3}, respectively. We assumed $\rho_{\rm m} = 0.9$ g cm^{-3}, $\tilde{h} = 0.1 - 0.2$, $\tau = 0.01$, and $\varepsilon_{\rm n} = 0.5$. The vertical dotted line indicates the semi-major axis corresponding to $\tilde{r}_{\rm h,m} = c_{\rm z}^{-1} \simeq 1.57$ assuming $\rho_{\rm m} = 0.9$ g cm^{-3}. The dashed line is drawn by Equation (3.12) for $\rho_{\rm mantle} = 0.28$ g cm^{-3} (from Yasui et al. 2014).

3.5 Effects of Ring Thickness on Particle Accretion

Next, we examine effects of ring thickness on the degree of particle accretion. As we described in Section 3.2, orbital inclinations of particles added to the simulation cell each timestep are assumed to follow Rayleigh distribution with a given value of r.m.s. inclinations, which is treated as a parameter, and orbital eccentricities are also given in a similar manner so that $\langle e_{\rm p}^2 \rangle^{1/2} = 2\langle i_{\rm p}^2 \rangle^{1/2}$.

Figure 3.9 illustrates the mass of the aggregate for the case of the partial coverage of the moonlet surface ($\tilde{r}_{\rm h,m} = 1.5$) as a function of time. The red, green and blue lines represent results with $\tilde{h} = 0.1$, 0.5 and 1, respectively. We find that the accretion rates increase with decreasing $\tilde{h}$ (i.e., decreasing $\langle e_{\rm p}^2 \rangle^{1/2}$ and $\langle i_{\rm p}^2 \rangle^{1/2}$) at the initial stage of $t \simeq 20 - 40\ T_{\rm K}$, because the lower impact velocities facilitate gravitational accretion at moonlet-particle collisions (Ohtsuki, 1993; Ohtsuki et al., 2013). However, the values of aggregate mass in the quasi-steady state is rather insensitive to ring thickness. Particles can accrete onto the high-latitude region of the moonlet surface directly when the ring thickness or the particle velocity dispersion is larger, but this does not lead to significant increase in the equilibrium mass of the aggregate, because impact velocities are large in this case and larger energy dissipation at collisions is required for accretion. Furthermore, because the high-latitude region of the moonlet surface overflows the Hill sphere in this case of $\tilde{r}_{\rm h,m} = 1.5$, particles cannot accrete on such areas and the mass and shape of the aggregate hardly depends on $\tilde{h}$.

Figure 3.10 shows aggregate mass growth in the case of $\tilde{r}_{\rm h,m} = 1.67$, where the entire surface of the moonlet is within the Hill sphere. First, we show the results for dilute rings with $\tau = 0.01$ (Figure 3.10(a)). In this case, when the ring is rather thin ($\tilde{h} = 0.2,\ 0.5$), the behavior of aggregate mass growth is similar to the case for $\tilde{r}_{\rm h,m} = 1.5$ (Figure 3.9), although the aggregate mass in the quasi-steady state is larger in the present case ($2 \lesssim m_{\rm agg}/m_{\rm m} \lesssim 4$) because of the larger Hill sphere. In such cases with $\tilde{h} < 1$, impacts mainly occur near the equatorial plane of the moonlet (Charnoz et al., 2007), and the aggregate near the equatorial plane grows

significantly, while particle accretion to the high-latitude region of the moonlet is inefficient. As a result, the aggregate tends to have a flattened shape. On the other hand, when the ring thickness is comparable to or larger than the moonlet radius ($\tilde{h} = 1,\ 2$), the aggregate grows significantly larger, with $m_{\rm agg}/m_{\rm m} \sim 7 - 9$ at most. In this case, particles can directly accrete to the high-latitude region of the moonlet surface. In many cases, we find that particles accumulate near either sub- or anti-Saturn side of the moonlet by the aid of the moonlet. Once such a temporary aggregate is formed around the moonlet, effective collision cross section is increased and the aggregate grows much larger than the moonlet, although it is not stable and large-scale mass shedding eventually takes place. In both cases of small and large ring thickness, significant radial shift (Δa) of the aggregate was observed; $\Delta a \lesssim 5R_{\rm m}$ for $\tilde{h} = 0.2 - 0.5$, and $\Delta a \lesssim 20R_{\rm m}$ for $\tilde{h} = 1 - 2$

If the rings are located sufficiently far from Saturn and their optical depth is sufficiently large, gravitational wakes or temporary gravitational aggregates can be formed (Salo, 1995; Kaljalainen & Salo, 2004), and it would also affect particle accretion onto moonlets. Figure 3.10(b) shows the growth of the aggregate mass in the case of $\tilde{r}_{\rm h,m} = 1.67$ and $\tau = 0.1$. One can see that the aggregate in the case of $\tilde{h} = 0.2$ significantly grows compared to the cases of $\tilde{h} = 0.5$ and 1. Figure 3.11 shows ring structures around the moonlet for the cases of various $\tilde{h}$ with $\tau = 0.1$. In the case of $\tilde{h} = 0.2$ shown in Figure 3.11(a), random velocity of particles is small enough to allow formation of gravitational wakes, and the wakes formed near the sub- and anti-Saturn sides of the moonlet help the formation of temporary particle aggregates there. Then, these accreted particles are shoved to the high-latitude region of the moonlet, resulting in the significant growth of the aggregate around the moonlet. Figure 3.12(a) shows a snapshot of the aggregate in the case of $\tilde{h} = 0.2$. One can see that a number of particles accumulate on the moonlet's surface and the temporary aggregate forms around the moonlet. In the cases of $\tilde{h} = 0.5$ and 1, notable gravitational wakes do not form because of higher random velocity of particles,

thus the growth of the aggregate is limited (Figures 3.10(b), 3.11(b), 3.11(c), and 3.12(b)). In the case of $\tilde{h} = 2$, on the other hand, the aggregate mass significantly increases, and then it reaches the quasi-steady state, repeating accretion and shedding of particles (Figure 3.10(b)). The moonlet can significantly grow in this case, because particles have sufficiently high orbital inclinations and can accrete directly onto the high-latitude region of the moonlet.

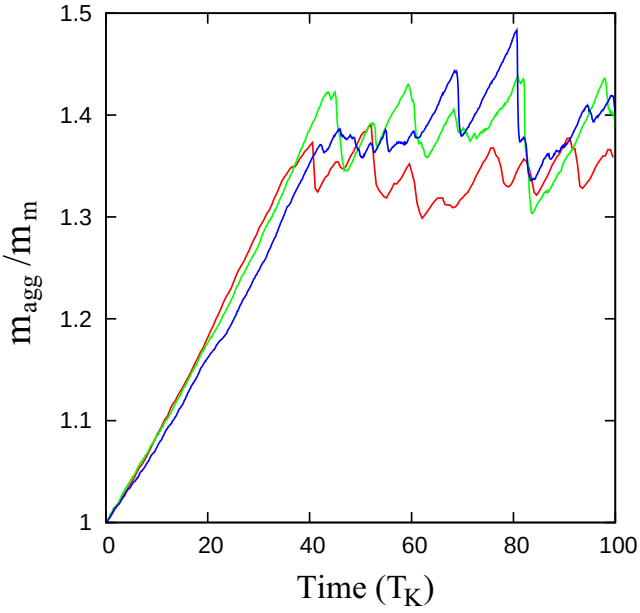

Figure 3.9: Evolution of the mass of the aggregate for the cases of $\tilde{r}_{\mathrm{h,m}} = 1.5$ with three different values of $\tilde{h}$. Red, green, and blue lines represent results with $\tilde{h} = 0.1$, 0.5 and 1, respectively. We assumed $\tilde{r} = 0.05$, $\tilde{\rho} = 1$, $\varepsilon_{\mathrm{n}} = 0.5$, and $\tau = 0.01$ (from Yasui et al. 2014).

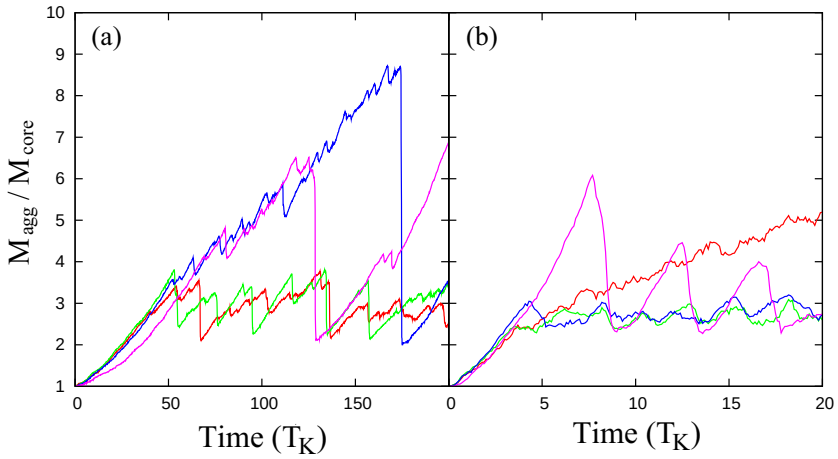

Figure 3.10: Evolution of the mass of the aggregate for the cases of $\tilde{r}_{\rm h,m} = 1.67$ with four different values of $\tilde{h}$. Panels (a) and (b) represent results with $\tau = 0.01$ and 0.1, respectively. Red, green, blue, and purple lines represent results with $\tilde{h} = 0.2$, 0.5, 1 and 2, respectively. We assumed $\tilde{r} = 0.15$, $\tilde{\rho} = 1$, and $\varepsilon_{\rm n} = 0.5$ (from Yasui et al. 2014).

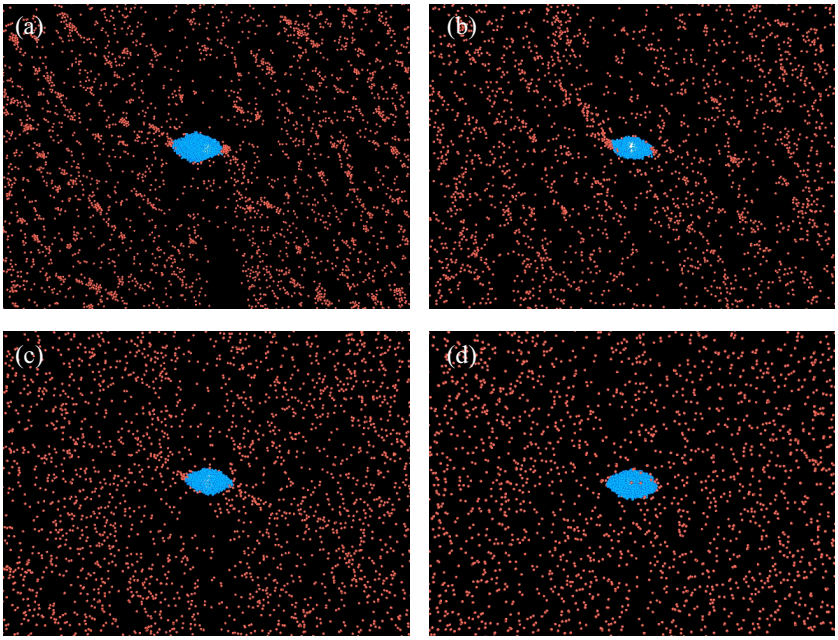

Figure 3.11: Snapshots of the spatial distribution of ring particles in the vicinity of the moonlet in the case of $\tilde{r}_{\rm h,m} = 1.67$ for four different values of $\tilde{h}$. Panels (a), (b), (c) and (d) show results with $\tilde{h} = 0.2$, 0.5, 1 and 2, respectively ($\tau = 0.1$). The rings are seen from the vertical direction against the plane of orbital motion. Saturn is to the left, and orbital motion is upward. A large white object at the center of each panel is the moonlet (which can be hardly seen because it is covered by particles). Blue particles are those regarded as members of the aggregate, while red ones are not (from Yasui et al. 2014).

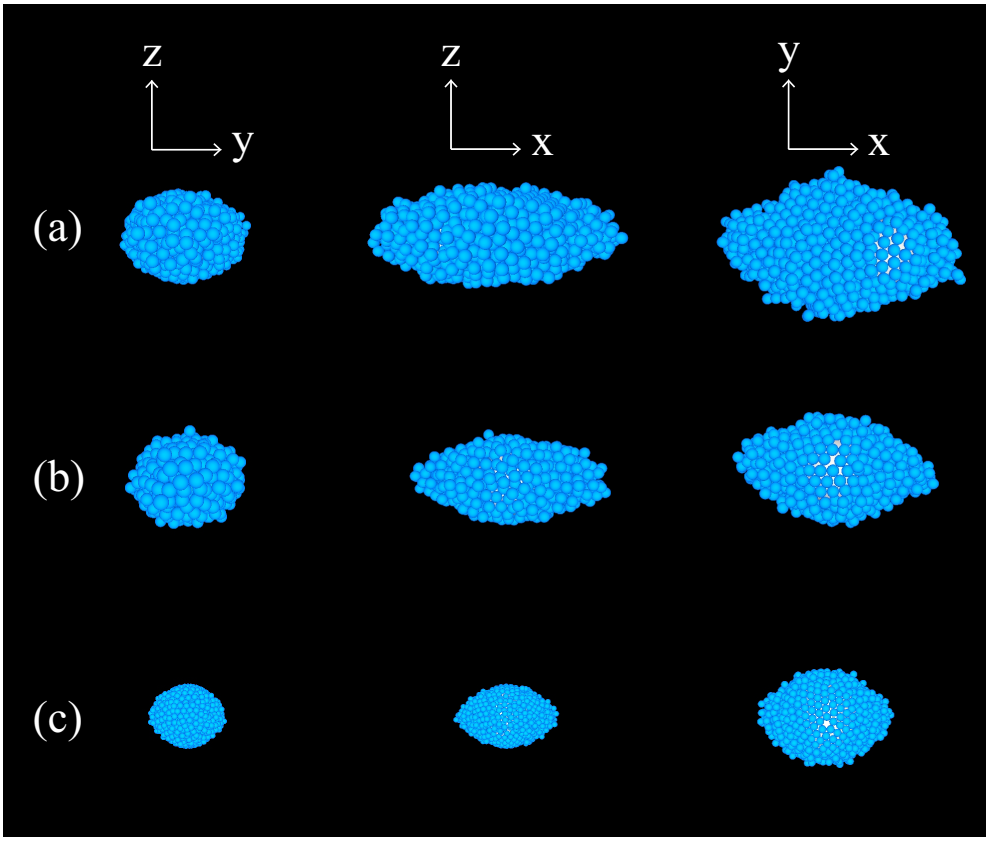

Figure 3.12: Snapshots of the distribution of particles accreted around the moonlet in the case of $\tilde{r}_{\rm h,m} = 1.67$ ($\varepsilon_{\rm n} = 0.5$). (a) $\tilde{\rho} = 1$, $\tilde{h} = 0.2$, and $\tau = 0.1$ ($\tilde{r} = 0.15$). (b) $\tilde{\rho} = 1$, $\tilde{h} = 1$, and $\tau = 0.1$ ($\tilde{r} = 0.15$). (c) $\tilde{\rho} = 0.33$, $\tilde{h} = 0.2$, and $\tau = 0.01$ ($\tilde{r} = 0.1$) (from Yasui et al. 2014).

3.6 Dependence on Other Parameters

3.6.1 Particle Density

Comparison between photometric modeling and observations of brightness asymmetry in Saturn's rings (e.g., Salo et al., 2004) and observations of the densities of small moons orbiting within or near the A ring (Porco et al., 2007) suggest that the internal density of ring particles is significantly smaller than the density of water ice (0.9 g cm^{-3}). However, actual densities of moonlets and ring particles are largely unknown. We performed simulations with several values of $\tilde{\rho}$ and examined effects of particle density on accretion. First, we describe the case of partial coverage of moonlet surface ($\tilde{r}_{\mathrm{h,m}} = 1.5$). Figures 3.13(a) and (b) show snapshots of the aggregates for the cases of $\tilde{\rho} = 0.33$ and 0.56 (see also Figure 3.7(a) for the case of $\tilde{\rho} = 1$). When $\tilde{\rho}$ is larger, particles can accrete even outside of the moonlet's Hill sphere due to the effect of mutual gravity between particles, and the aggregate tends to have a shape extended toward the x-axis (Figure 3.7(a)). At the time of mass shedding in this case, a number of particles are removed together in a form of elongated aggregate due to the effect of self-gravity of leaving particles, thus particles accreted near the equatorial plane or at the high-latitude region are replaced repeatedly. On the other hand, when particles' internal density is smaller, the tendency of particle accumulation near the sub- and anti-Saturn sides of the moonlet is weakened, and the shape of the equator of the aggregate becomes rounder (Figure 3.13(a)). Particles tend to leave the aggregate as individual particles rather than a group when $\tilde{\rho}$ is small. In spite of such differences in aggregate shape and mass shedding, the number of particles in an aggregate in the quasi-steady state was found to be approximately the same, and the mass of the mantle (i.e., $m_{\mathrm{agg}} - m_{\mathrm{m}}$) was nearly proportional to $\tilde{\rho}$. This reflects the fact that the volume of the moonlet's Hill sphere outside the moonlet surface is rather small in the present case, and the effect of self-gravity of accreted particles on mass accretion is limited.

Next, we examine the dependence of $\tilde{\rho}$ in the case of complete coverage of moonlet

surface. Figure 3.14 shows the evolution of the mass of the aggregate and particle number in the aggregate in the cases of $\tilde{r}_{\rm h,m} = 1.67$ for four values of $\tilde{\rho}$. We find that both aggregate mass and particle number in the aggregate are larger when $\tilde{\rho}$ is large, and that significant mass shedding takes place for large values of $\tilde{\rho}$. The snapshot of the aggregate in the case of $\tilde{r}_{\rm h,m} = 1.67$ and $\tilde{\rho} = 0.33$ in Figure 3.12(c) shows that the shape of the equatorial plane of the aggregate is rounder compared to the cases shown in Figures 3.12(a) and (b), because of the weaker effect of the self-gravity of accreted particles. These results show that the internal density of accreting particles would significantly affect the shape of aggregates.

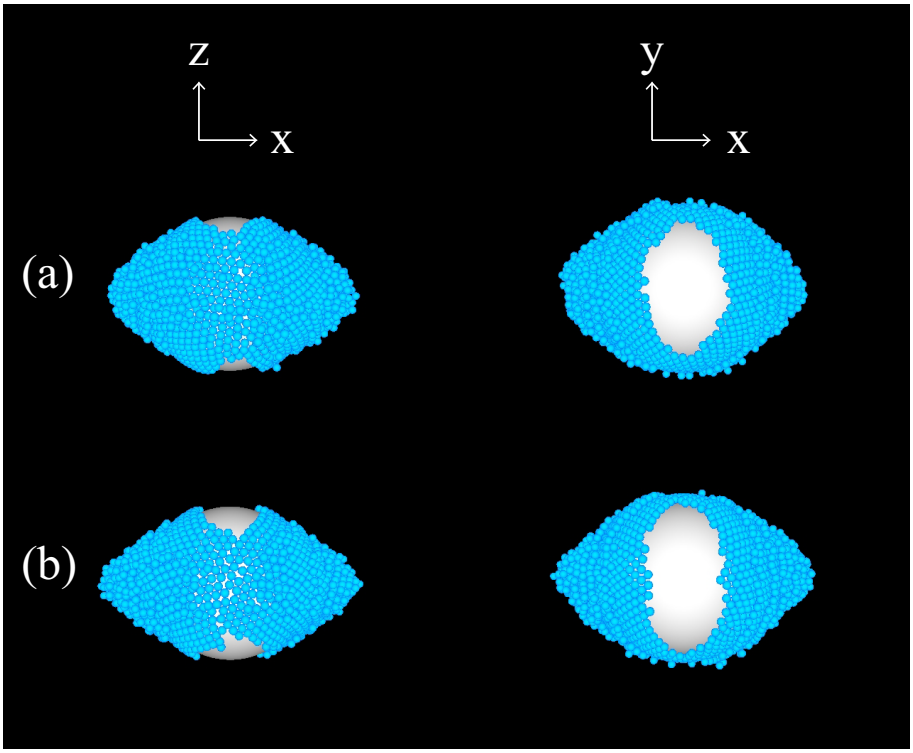

Figure 3.13: Snapshots of the distribution of particles accreted around the moonlet in the case of $\tilde{r}_{\rm h,m} = 1.5$ for two different values of $\tilde{\rho}$. Panels (a) and (b) represent cases with $\tilde{\rho} = 0.33$ and 0.56, respectively. We assumed $\tilde{r} = 0.05$, $\tilde{h} = 0.1$, $\tau = 0.01$, and $\varepsilon_{\rm n} = 0.5$ (from Yasui et al. 2014).

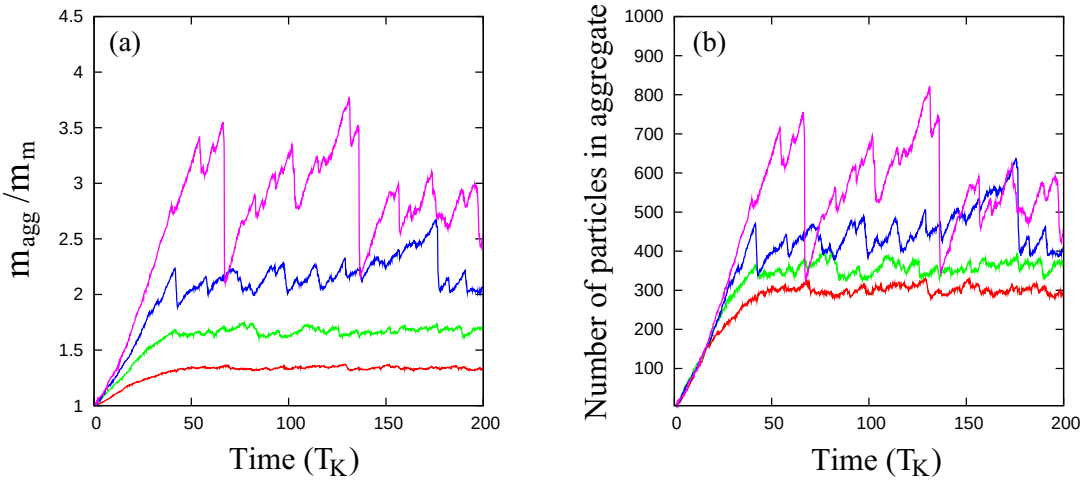

Figure 3.14: Evolution of the mass of the aggregate (Panel (a)) and the number of particles in the aggregate (Panel (b)) in the case of $\tilde{r}_{\mathrm{h,m}} = 1.67$ for four values of $\tilde{\rho}$. Red, green, blue and purple lines indicate results with $\tilde{\rho} = 0.33$, 0.56, 0.78, and 1, respectively. We assumed $\tilde{r} = 0.15$, $\tilde{h} = 0.2$, $\tau = 0.01$, and $\varepsilon_{\mathrm{n}} = 0.5$ (from Yasui et al. 2014).

3.6.2 Particle Size Distribution

So far we have assumed that ring particles have identical sizes, but actual ring particles have a size distribution. Here we examine the effect of particle size distribution on accretion onto moonlets. We assume that particles have a differential power-law size distribution with an exponent of -3, which is suggested by observations (Zebker et al., 1985; French & Nicholson, 2000). In our simulations, particle sizes are given ranging from 30 cm ($R_{\rm min}$) up to 5 m ($R_{\rm max}$) following Porco et al. (2007), where $R_{\rm min}$ and $R_{\rm max}$ denote the radii of the smallest and largest particle, respectively (Appendix D). We assume $R_{\rm m} = 1250$ cm for the radius of the moonlet.

Figure 3.15 shows the mass of the aggregate as a function of time, for four combinations of $\tilde{r}_{\rm h,m}$ and τ: (a) $\tilde{r}_{\rm h,m} = 1.5$ with $\tau = 0.1$, (b) $\tilde{r}_{\rm h,m} = 1.5$ with $\tau = 0.5$, (c) $\tilde{r}_{\rm h,m} = 1.69$ with $\tau = 0.1$, and (d) $\tilde{r}_{\rm h,m} = 1.69$ with $\tau = 0.5$, respectively. In these figures, red and green lines indicate results with a uniform particle and those with the particle size distribution, respectively. Although the difference between the two results is rather small in the case of Panel (d), we find that the degree of particle accretion tends to be smaller when particle size distribution is included. This seems to be explained by the following three reasons. (1) Because the size of the largest particle in the size distribution is significant compared to the moonlet size ($R_{\rm max}/R_{\rm m} = 0.4$), impacts of such larger particles often disrupt the mantle of the aggregate; (2) When a large particle is leaving the aggregate at the time of mass shedding, it is accompanied by many other particles because of its strong gravity; and (3) Mechanisms of particle migration and accretion to the high-latitude region on the moonlet surface become inefficient, because larger particles in the size distribution have small orbital inclinations and cannot accrete onto the high-latitude region. Accretion of smaller particles onto the high-latitude region still takes place but becomes difficult, because now there are less particles at the high-latitude regions that could hold these small ones there.

The snapshots of the aggregate in the quasi-steady state for each case are shown in

Figure 3.16. One can see that smaller particles tend to accrete to the high-latitude region of the moonlet (see also Porco et al., 2007). In the case with high optical depth, the mantle of the aggregate is connected with the ring around the aggregate and extended in the shear direction (Lewis & Stewart, 2009). In the case with high optical depth, collisions of large particles onto the aggregate occur frequently, and collisions of a group of particles often shove already-accreted particles to the high-latitude region. Through such mechanisms, larger particles sometimes migrate to the high latitude region of the moonlet surface.

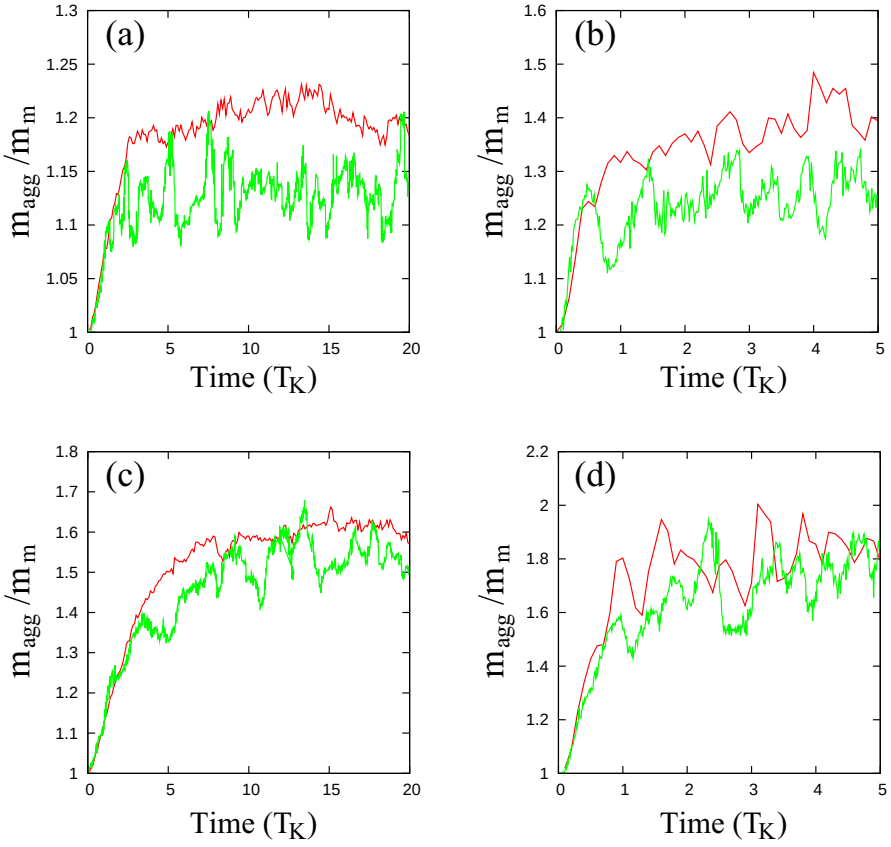

Figure 3.15: Comparison between results with and without particle size distribution for the evolution of the mass of the aggregate. Red and green lines represent the results with identical particles ($R_{\rm uni} = 167$ cm; Appendix D) and including a particle size distribution ($q = 3$, $R_{\rm max} = 500$ cm, and $R_{\rm min} = 30$ cm), respectively. Four cases with different combinations of $\tilde{r}_{\rm h,m}$ and τ are shown: (a) $\tilde{r}_{\rm h,m} = 1.5$ with $\tau = 0.1$, (b) $\tilde{r}_{\rm h,m} = 1.5$ with $\tau = 0.5$, (c) $\tilde{r}_{\rm h,m} = 1.69$ with $\tau = 0.1$, and (d) $\tilde{r}_{\rm h,m} = 1.69$ with $\tau = 0.5$. We assumed $\tilde{\rho} = 0.44$, $R_{\rm m} = 1250$ cm, and $\varepsilon_{\rm n} = 0.5$ (from Yasui et al. 2014).

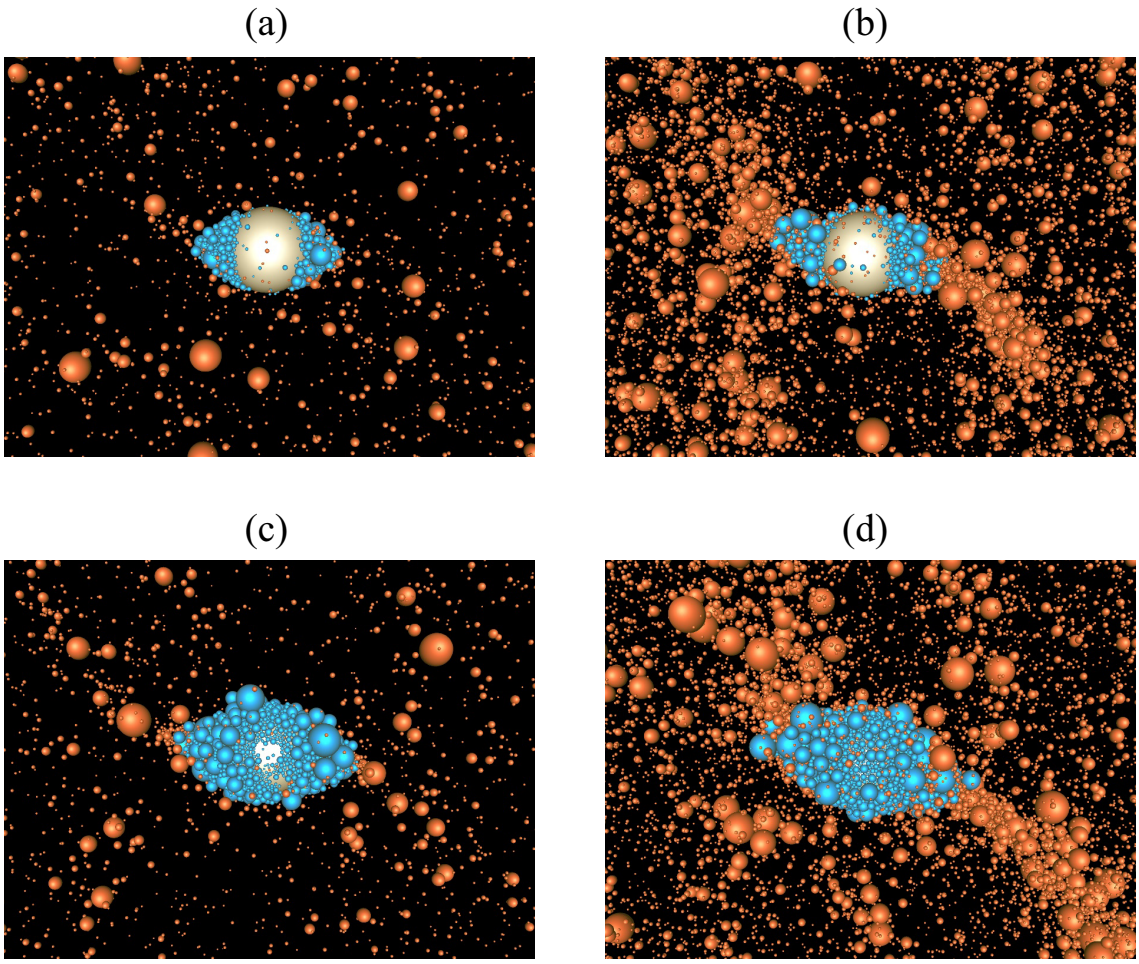

Figure 3.16: Snapshots of the spatial distribution of particles in the vicinity of the moonlet in the case with particle size distribution. Panels (a) to (d) represent results for the cases shown in Panels (a) to (d) in Figure 3.15, respectively. The rings are seen from the vertical direction against the plane of orbital motion. Saturn is to the left, and orbital motion is upward. A large white object is the moonlet. Blue particles are those regarded as members of particles in the aggregate, while red ones are not (from Yasui et al. 2014).

3.7 Conclusions and Discussion

In the present work, using local N-body simulation, we studied gravitational accretion of ring particles onto moonlets in Saturn's rings. If the internal density of a moonlet is that of water ice, the moonlet overflows its Hill sphere at radial locations interior to the Cassini Division. In this case, particles can accrete only part of the moonlet surface, and the degree of particle accretion decreases with decreasing distance from Saturn. We found that accretion of porous particles onto moonlets with density of water ice becomes negligible within the radial location of the inner B ring. Although the critical distance shifts to the outer edge of the C ring if the density of ring particles is as high as that of water ice, modeling and observations of the rings' brightness asymmetry as well as observations of the densities of small ringmoons suggest that such a high density is unlikely. Thus, our results suggest that gravitational accretion of ring particles onto moonlets is unlikely to occur at radial locations interior to the outer edge of the C ring, unless the density of the moonlets is much larger than that of water ice or non-gravitational cohesive forces play a major role. We examined accretion process of individual particles onto moonlets from detailed analysis of snapshots of our numerical results, and found that particle accretion onto the high-latitude regions of the moonlet occurs even if the vertical extent of particle motion is much smaller than the moonlet's radius. In the inner rings where a moonlet's Hill sphere partially covers its surface, particles can accrete onto the high-latitude regions of the moonlet through migration on the surface caused by collisions of other particles. In the outer region of the rings where particles can cover the entire surface of the moonlet, those particles already accreted near the equator of the moonlet are shoved to the high-latitude regions by further accretion. In the case of the inner rings, the degree of particle accretion hardly depends on the ring thickness because the volume of its Hill sphere within which particles can accrete is rather limited. On the other hand, in the case of outer rings with low optical depth ($\tau \sim 0.01$), large temporary aggregates tend to be formed around moonlets when

the vertical thickness of the ring is large and particles can accrete directly onto the high-latitude region of moonlets. If the rings are vertically thin and have larger optical depth ($\tau \sim 0.1$), gravitational wakes or temporary particle aggregates are formed and particles tend to accumulate either sub- or anti-Saturn side of a moonlet to form large temporary aggregates. On the other hand, if such rings with larger optical depth have large vertical thickness, gravitational wakes or temporary aggregates do not form because of high random velocity, and particles accrete onto moonlets nearly symmetrically to form large aggregates. We also found that the shape of moonlets' equatorial plane becomes rounder when the particle density is low, and that the degree of particle accretion including particle size distribution is smaller than the case with identical particles.

Pan and Daphnis form gaps in the outer A ring, and the cores of these moons may be large collisional shards created when rings were formed. The cores would have grown by accretion of ring particles and formed gaps, which then would have stopped further particle accretion onto the cores (Porco et al., 2007). It has been suggested that these small moons (Pan, Daphnis and Atlas) would have had shapes similar to the Hill sphere when the ring thickness was large, and then their equatorial ridge would have been formed by particle accretion after the rings became thin before complete gaps were formed (Porco et al., 2007; Charnoz et al., 2007). However, our results in the present work show that particles can accrete onto the high-latitude region of moonlets, even if the thickness of the rings is much smaller than the radius of the moonlet. This implies that the main bodies of Pan, Daphnis and Atlas with a Hill-sphere shape might have been formed in rather thin rings.

On the other hand, impacts of particles onto the equatorial plane are important to form the equatorial ridges of Pan and Atlas (Charnoz et al. 2007). Observations show that the equatorial planes of Pan and Atlas are rounder than that of the Hill sphere. Our numerical results show that the equatorial planes of aggregates become rounder in cases with the lower internal density of particles, because of the reduced effects

of particles' mutual gravity. If such equatorial ridges were formed by gravitational accretion of particles before the moonlet's Hill sphere was filled by accreting particles, formation of the ridges and their rounder shapes may be explained by accretion of low-density particles. On the other hand, if particles already filled most part of the aggregate's Hill sphere before ridge formation, the ridges cannot be formed by gravitational accretion. In this case, we need to consider non-gravitational adhesive forces (e.g., Albers & Spahn, 2006) for the formation of the equatorial ridges.

Observations of Saturn's rings by the Cassini spacecraft revealed the existence of boulders and moonlets that are much larger than the background particles (e.g., Tiscareno et al. 2006, 2008, 2010; Sremčević et al. 2007, 2011; Esposito et al. 2008; Meinke et al. 2012; Baillié et al. 2013). Most of them were inferred from observations of propeller structures found in the A ring, and also from the recent report on the detection of a similar structure in the B ring (Sremcevic et al. 2011). On the other hand, the existence of boulders in the C ring has also been recently suggested from the observations of transparent holes (Baillie et al. 2013). Our numerical results show that gravitational accretion of particles onto moonlets is negligible at radial locations interior to the outer edge of the C ring, unless the density of the moonlets is much larger than that of water ice. This implies that these boulders might be the largest collisional shards placed in such locations when or after the rings formed, although their growth by particle accretion due to non-gravitational cohesive forces cannot be ruled out. Furthermore, the observations of transparent holes infer the existence of boulders in the Cassini Division. From our results, if dense cores ($\rho_{\rm m} \sim 0.9$ g cm^{-3}) exist in the Cassini Division, the aggregate mass can become at most twice as much as the moonlet's mass by gravitational accretion of small ring particles, although the final mass depends on the density of particles. Thus, large boulders (~ 10 m) in the Cassini Division may be gravitational aggregates formed by particle accretion onto dense cores. Also in the A ring many propeller moonlets are found, which may be gravitational aggregates formed by particle accretion as well. The results of our

present work combined with more detailed observations about the number and radial distribution of moonlets and boulders in Saturn's rings would provide constrains on the rings' history, such as breakup events of the rings' progenitor bodies and their subsequent evolution.

Chapter 4

Summary

We examined viscosity in self-gravitating planetary rings in Chapter 2 and also gravitational accretion of ring particles onto moonlets in Saturn's rings in Chapter 3, using local N-body simulation.

In Chapter 2, we examined viscosity in self-gravitating planetary rings. We investigated dependence of viscosity on various parameters in detail, including effects of particles' surface friction. In the case of self-gravitating rings with low optical depth, we found that viscosity is determined by particles' random velocity. Inclusion of surface friction slightly reduces both random velocity and viscosity when particles' random velocity is determined by inelastic collisions. On the other hand, surface friction slightly increases viscosity when gravitational encounters play a major role in particle velocity evolution, so that viscous heating balances with increased energy dissipation at collisions due to surface friction. We found that inclusion of surface friction changes viscosity in dilute rings up to a factor of about two. In the case of self-gravitating dense rings, viscosity is increased significantly due to effects of gravitational wakes (Daisaka et al. 2001), and we found that varying restitution coefficients changes viscosity in such dense rings also by a factor of about two. We confirmed that our numerical results for viscosity in dense rings with gravitational wakes can be well approximated by a semianalytic expression that is consistent with a previously obtained formula. However, we found that this formula seems to overestimate viscosity in dense rings far from the central planet, where temporary gravi-

tational aggregates form. Thus, we derived a revised expression for such a case. We confirmed that the semianalytic expressions we obtained reproduce our numerical results well for the entire range of parameters examined here. On the other hand, temporary aggregates are likely to be formed in the outer A ring (e.g., Salo, 1995; Kaljalainen & Salo, 2004). Recent models of the formation of Saturn's small moons orbiting just outside the main rings suggest that these small moons likely formed by accretion of particles radially spreading from the ring (Charnoz et al., 2010; Canup, 2010). Thus, it is important to clarify viscosity in rings with temporary aggregates.

In Chapter 3, we examined gravitational accretion of ring particles onto moonlets in Saturn's rings. We found that gravitational accretion of ring particles onto moonlets is unlikely to occur at radial locations interior to the outer edge of the C ring, unless the density of the moonlet is much larger than that of solid water ice or non-gravitational cohesive forces play a major role. We found that the degree of mass increase of moonlets ($m_{\rm agg}/m_{\rm m}$) by accretion of particles with $\rho_{\rm p} = 0.4$ g cm^{-3} is $\lesssim 1.3$ in the outer B ring and ~ 1.5 in the mid-A ring., the latter being consistent with the previous study (Porco et al., 2007). We also examined accretion process of individual particles onto moonlets in detail, and found that particle accretion onto the high-latitude regions of the moonlet surface occurs even if the vertical thickness of the ring is much smaller than the moonlet's radius. In inner rings where a moonlet's Hill sphere partially covers its surface, migration of particles to the high-latitude regions is caused by collisions of other particles, while in the case of outer regions of the rings where particles can cover the entire surface of the moonlet, particles already accreted near the equator of the moonlet can be shoved to the high-latitude regions by further accretion. The degree of particle accretion in outer rings is found to depend significantly on ring's vertical thickness and optical depth. We also examined effects of the internal density of accreting particles, and found that the shape of moonlets' equator becomes rounder when particle density is lower. Furthermore, we found that the degree of particle accretion including particle size distribution

is smaller than the case with identical particles. Our results imply that the main bodies of Pan, Daphnis and Atlas with a Hill-sphere shape might have been formed in rather thin rings. Our results suggest that larger boulders recently inferred from observations of transparent holes in the C ring are likely to be collisional shards, while propeller moonlets in the A ring would be gravitational aggregates formed by particle accretion. The results of our present work combined with more detailed observations about the number and radial distribution of moonlets and boulders in Saturn's rings would provide constrains on the rings' history, such as breakup events of the rings' progenitor bodies and their subsequent evolution.

Appendix

Appendix A
Changes in Particle Velocity and Rotation Rate Due to Collision

When two particles, i and j, collide with each other, the changes of their velocities and rotation rates are calculated as follows. We assume that ring particles are spheres, and we let the mass, radius, and spin angular velocity vector of particle j be given by m_j, R_j, and $\boldsymbol{\omega}_j$, respectively. Suppose that two particles, i and j, collide with each other with relative velocity of the centers of the two bodies in the rotating coordinate system, $\boldsymbol{v}$, and that their relative position at impact is given by $\boldsymbol{r}$. Let $\boldsymbol{v}_{\rm n}$ and $\boldsymbol{v}_{\rm t}$ denote the normal and the tangential component of $\boldsymbol{v}$ to the tangent plane, respectively. In this case, the normal and the tangential components of the relative velocity of the two contacting points at the time of impact can be written as (e.g., Araki & Tremaine, 1986; Richardson, 1994; Ohtsuki, 2006a,b)

$$\begin{aligned} \boldsymbol{u}_{\rm n} &= \boldsymbol{v}_{\rm n} = (\boldsymbol{v}\cdot\boldsymbol{\lambda})\boldsymbol{\lambda}, \\ \boldsymbol{u}_{\rm t} &= \boldsymbol{v}_{\rm t} + \boldsymbol{\Omega}\times\boldsymbol{r} + \boldsymbol{\lambda}\times(R_i\boldsymbol{\omega}_i + R_j\boldsymbol{\omega}_j), \end{aligned} \tag{A1}$$

where $\boldsymbol{\lambda} \equiv \boldsymbol{r}/|\boldsymbol{r}|$ is the unit vector pointing from the center of particle i to that of particle j, and $\boldsymbol{\Omega} \equiv (0, 0, \Omega)$ is the Keplerian angular velocity vector of the coordinate system. In the above equation, we used the relation $\boldsymbol{r} = (R_i + R_j)\boldsymbol{\lambda}$ at impact. In terms of the normal and the tangential restitution coefficients, $\varepsilon_{\rm n}$ and $\varepsilon_{\rm t}$, the normal and the tangential components of the relative velocity of the two contacting points after impact are given by Equation (2.2). From Equation (2.2) and the conservation of linear and angular momenta, the change of the normal and the tangential

components of the relative velocity of the centers of the two spheres are given as

$$\begin{aligned} \Delta \boldsymbol{v}_{\rm n} &= -(1+\varepsilon_{\rm n})\boldsymbol{v}_{\rm n}, \\ \Delta \boldsymbol{v}_{\rm t} &= -\frac{\mathcal{K}}{\mathcal{K}+1}(1-\varepsilon_{\rm t})\{\boldsymbol{v}_{\rm t} + R_{\rm p}\boldsymbol{\lambda}\times(\boldsymbol{\omega}-\boldsymbol{\Omega})\}, \end{aligned} \tag{A2}$$

where $R_{\rm p} \equiv R_i + R_j$ and

$$\boldsymbol{\omega} \equiv (R_i\boldsymbol{\omega}_i + R_j\boldsymbol{\omega}_j)/(R_i+R_j). \tag{A3}$$

In the above, $\mathcal{K}$ is the coefficient of the moment of inertia, e.g., $I_j = \mathcal{K}m_jR_j^2$. In the present work, we set $\mathcal{K} = 2/5$, assuming a homogeneous sphere. The change of spin angular velocity of particle j due to the collision is written as

$$\Delta\boldsymbol{\omega}_j = \frac{\mu(1-\varepsilon_{\rm t})}{(\mathcal{K}+1)m_jR_j}\boldsymbol{\lambda}\times\{\boldsymbol{v}_{\rm t} + R_{\rm p}\boldsymbol{\lambda}\times(\boldsymbol{\omega}-\boldsymbol{\Omega})\}, \tag{A4}$$

where μ is the reduced mass.

Appendix B
Energy Dissipation Due to an Inelastic Collision Between Particles

When a local ring region is in a quasisteady state, its average viscosity can be calculated by summing up the amount of energy dissipated at collisions that occur in the region during a certain time interval (Equation (2.4)). Following Tanaka et al. (2003, their Equation (43)), we calculate the amount of energy dissipated at a collision between particles j and k as

$$\Delta E_{{\rm col},jk} = -\frac{1}{2}\mu h^2 a_0^2\Omega^2\left(\Delta\tilde{e}^2_{{\rm col},jk} + \Delta\tilde{i}^2_{{\rm col},jk} - \frac{3}{4}\Delta\tilde{b}^2_{{\rm col},jk}\right). \tag{B1}$$

In the above, $\mu = (1/m_j + 1/m_k)^{-1}$ (m_j is the mass of particle j, and $m_j = m$ in the equal-sized case studied in the present work); $h = (2m/3M_c)^{1/3}$; and $\Delta\tilde{e}^2_{{\rm col},jk}$, $\Delta\tilde{i}^2_{{\rm col},jk}$ and $\Delta\tilde{b}^2_{{\rm col},jk}$ are the changes in the square of the scaled relative orbital elements $\tilde{e}$, $\tilde{i}$, and $\tilde{b}$ due to the collision, where $\tilde{e}$ and $\tilde{i}$ are the eccentricity and the inclination of the relative motion scaled by h (see Ohtsuki, 1999), and $\tilde{b}$ is the difference in the semimajor axes of the two particles scaled by ha_0. Note that the effects of time

variation of the total self-gravitational energy, random kinetic energy, or rotational energy of particles do not appear in Equation (B1) because we assume the region is in a quasisteady state.

Appendix C
The axial ratios of the Hill sphere

Under Hill's approximation, the potential U for the relative motion of two bodies in orbit about the central body with orbital angular frequency Ω can be written as (e.g., Nakazawa & Ida, 1988; Ohtsuki, 2012)

$$U = -\frac{\Omega^2}{2}\left(3x^2 - z^2\right) - \frac{G\left(m_1 + m_2\right)}{r} + \frac{9}{2}R_{\rm H}^2\Omega^2, \tag{C1}$$

where $r = \left(x^2 + y^2 + z^2\right)^{1/2}$, and $R_{\rm H}$ is the mutual Hill radius of the two bodies. In the above, the first term accounts for the tidal potential, the second term represents the mutual gravity between the two bodies, and the constant $(9/2)\,R_{\rm H}^2\Omega^2$ has been added so that $U = 0$ at the Lagrangian points $(x,\ y,\ z) = (\pm R_{\rm H},\ 0,\ 0)$. Thus, the Hill sphere represents the region surrounded by the $U = 0$ contour surface. If the radial, azimuthal, and vertical semi-axes of the Hill sphere are denoted by $c_x R_{\rm H}$, $c_y R_{\rm H}$ and $c_z R_{\rm H}$, $c_x = 1$ as mentioned above, and we can easily obtain $c_y = 2/3$ by substituting $x = z = 0$ and $U = 0$ into Equation (C1). In order to obtain c_z, on the other hand, we have to solve a cubic equation as follows. Substituting $x = y = 0$, $z = c_z R_{\rm H}$, and $U = 0$ into Equation (C1), we have

$$c_z^3 + 9c_z - 6 = 0. \tag{C2}$$

This can be solved by Cardano's method, as follows. Letting $c_z = u + v$, where u and v are new variables, Equation (C2) can be rewritten as

$$u^3 + v^3 + 3\left(u + v\right)\left(uv + 3\right) - 6 = 0. \tag{C3}$$

Equation (C3) is satisfied when

$$u^3 + v^3 = 6 \quad \text{and} \quad \left(uv + 3\right)\left(u + v\right) = 0. \tag{C4}$$

Because $c_z = u + v \neq 0$, we have $v = -3/u$ from the second equation of (C4). Substituting this into the first equation of (C4), we have

$$u^6 - 6u^3 - 27 = 0. \tag{C5}$$

Setting $X = u^3$, Equation (C5) becomes a quadratic equation for X, which can be easily solved to obtain the positive solution $X = 9$. Therefore, we finally obtain $u = 3^{2/3}$ and $v = -3^{1/3}$, i.e.,

$$c_z = 3^{2/3} - 3^{1/3} \simeq 0.638. \tag{C6}$$

Therefore, the axial ratios of the Hill sphere are given by

$$c_x : c_y : c_z = 1 : \frac{2}{3} : \left(3^{2/3} - 3^{1/3}\right) \simeq 1 : \frac{2}{3} : 0.638. \tag{C7}$$

Appendix D
Particle size distribution used in numerical simulation

In our simulations with particle size distribution, we assumed the following power law distribution;

$$n\,(R)\,dR = C_0 R^{-q} dR, \tag{D1}$$

where $n\,(R)$ is the number of particles with radius between R and $R + dR$, and C_0 is a constant. Spacecraft and ground-based observations (e.g., Zebker et al., 1985; French & Nicholson, 2000) suggest that $q \simeq 3$, $R_{\rm min} \simeq 0.1$ cm, and $R_{\rm max} \simeq 20$ m in Saturn's main rings. However, the width of the above actual size distribution is too large for N-body simulations, and we need to truncate it to a narrow width. In the present work, we adopt $q = 3$, $R_{\rm min} = 30$ cm, and $R_{\rm max} = 5$ m, following Porco et al. (2007). In order to examine effects of including size distribution, we compare results with the case of particles with a uniform radius $R_{\rm uni}$, where $R_{\rm uni}$ is determined so that the optical depth and the surface density become equal to the case with size distribution (Morishima & Salo, 2006). When $q = 3$, the surface density of a system including the size distribution is given as

$$\Sigma_{\rm size} = \frac{4}{3}\rho_{\rm p}\tau R_{\rm max}\frac{1 - W^{-1}}{\ln W}, \tag{D2}$$

where $W = R_{\rm max}/R_{\rm min}$. Because the surface density in the case of a uniform size is $\Sigma_{\rm uni} = 4\rho_{\rm p}\tau R_{\rm uni}/3$, we have $\Sigma_{\rm uni} = \Sigma_{\rm size}$ when $R_{\rm uni} = R_{\rm max}\left(1 - W^{-1}\right)/\ln W$. In the present case, we obtain $R_{\rm uni} \simeq 167$ cm.

Acknowledgments

First of all, I wish to thank my supervisor, Prof. Keiji Ohtsuki, for a lot of helpful advice and fruitful discussions during my thesis work. I would also like to thank my collaborator, Prof. Hiroshi Daisaka for his help in numerical simulations. I also thank Prof. Yoshitsugu Nakagawa and Yuri Aikawa, and other members of the Planetary Astrophysics Group at Kobe University for their discussion. A portion of the numerical simulations presented in Chapters 2 and 3 was performed using the GRAPE-7 system at the Center for Computational Astrophysics of the National Astronomical Observatory of Japan. I greatly appreciate the Research Fellowship from the Japan Society for the Promotion of Science (JSPS) for Young Scientists.

Bibliography

Albers, N., & Spahn, F., 2006. The influence of particle adhesion on the stability of agglomerates in Saturn's rings. Icarus 181, 292-301.

Araki, S., & Tremaine, S., 1986. The dynamics of dense particle disks. Icarus 65, 83-109.

Baillié, K., Colwell, J.E., Esposito, L.W., & Lewis, M.C., 2013. Meter-sized moonlet population in Saturn's C ring and Cassini Division. Astron. J. 145, 171.

Borderies, N., Goldreich, P., & Tremaine, S., 1985. A granular flow model for dense planetary rings. Icarus 63, 406-420.

Bridges, F., Hatzes, A., & Lin, D., 1984. Structure, stability, and evolution of Saturn's rings. Nature 309, 333-338.

Canup, R.M., 2010. Origin of Saturn's rings and inner moons by mass removal from a lost Titan-sized satellites. Nature 468, 943-946.

Canup, R.M., & Ward, W.R., 2002. Formation of the Galilean satellites: Conditions of accretion. Astron. J. 124, 3404-3423.

Chandrasekhar, S., 1969. Ellipsoidal Figures of Equilibrium. The Silliman Foundation Lectures. Yale Univ. Press, New Haven.

Charnoz, S., Brahic, A., Thomas, P.C., & Porco, C.C., 2007. The equatorial ridges of Pan and Atlas: Terminal accretionary ornaments? Science 318, 1622-1624.

Charnoz, S., Morbidelli, A., Dones, L., & Salmon, J., 2009. Did Saturn's rings form during the late heavy bombardment? Icarus 199, 413-428.

Charnoz, S., Salmon, J., & Crida, A., 2010. The recent formation of Saturn's moonlets from viscous spreading of the main rings. Nature, 465, 752-754.

Colwell, J.E., Nicholson, P.D., Tiscareno, M.S., Murray, C.D., French, R.G., Marouf, E.A. et al., 2009. The structure of Saturn's rings. In: Dougherty, M.K., Esposito, L.W., Krimigis, S.M. (Eds.), Saturn from Cassini-Huygens. Springer, pp. 375-412.

Cuzzi, J., Clark, R., Filacchione, G., French, R., Johnson, R., Marouf, E., & Spilker, L., 2009. Ring particle composition and size distribution. In: Dougherty, M.K., Esposito, L.W., Krimigis, S.M. (Eds.), Saturn from Cassini-Huygens. Springer, pp. 535-573.

Daisaka, H., & Ida, S., 1999. Spatial structure and coherent motion in dense planetary rings induced by self-gravitational instability. Earth Planets Space 51, 1195-1213.

Daisaka, H., Tanaka, H., & Ida, S., 2001. Viscosity in a dense planetary ring with self-gravitating particles. Icarus 154, 296-312.

Dones, L., 1991. A recent cometary origin for Saturn's rings? Icarus 92, 194-203.

Dones, L., Agnor, C.B., & Asphaug, E., 2007. Formation of Saturn's rings by tidal disruption of a Centaur. BAAS 38 420.

Esposito, L.W., 1986. Structure and evolution of Saturn's rings. Icarus 67, 345-357.

Esposito, L.W., Harris, C.C., & Simmons, K.E., 1987. Features in Saturn's rings. Astrophys. J. Suppl. 63, 749-770.

Esposito, L.W., Ocallaghan, M., & West, R.A., 1983. The structure of Saturn's rings: Implications from the Voyager stellar occultation. Icarus 56, 439-452.

Esposito, L.W., Meinke, B.K., Colwell, J.E., Nicholson, P.D., & Hedman, M.M., 2008. Moonlets and clumps in Saturn's F ring. Icarus 194, 278-289.

French, R.G., & Nicholson, P.D., 2000. Saturn's rings. II. Particle sizes inferred from stellar occultation data. Icarus 145, 502-523.

Goldreich, P., & Tremaine, S., 1978. The velocity dispersion in Saturn's rings. Icarus 34, 227-239.

Goldreich, P., & Tremaine, S., 1982. The dynamics of planetary rings. Annu. Rev. Astron. Astrophys. 20, 249-283.

Harris, A.W., 1984. The origin and evolution of planetary rings. In: Greenberg, R., Brahic, A. (Eds.), Planetary Rings. Univ. of Arizona Press, Tucson, pp. 641-659.

Holberg, J.B., Forrester, W.T., & Lissauer, J.J., 1982. Identification of resonance features within the rings of Saturn. Nature 297, 115-120.

Karjalainen, R., 2007. Aggregate impacts in Saturn's rings. Icarus 189, 523-537.

Karjalainen, R., & Salo, H., 2004. Gravitational accretion of particles in Saturn's rings. Icarus 172, 328-348.

Leinhardt, Z.M., Ogilvie, G.I., Latter, H.N., & Kokubo, E. 2012. Tidal disruption of satellites and formation of narrow rings. Mon. Not. R. Astron. Soc. 424, 1419-1431.

Lewis, M.C., & Stewart, G.R., 2009. Features around embedded moonlets in Saturn's rings: The role of self-gravity and particle size distributions. Icarus 199, 387-412.

Lynden-Bell, D., & Kalnajs, A.J., 1972. On the generating mechanism of spiral structure. Mon. Not. R. Astron. Soc. 157, 1-30.

Marouf, E.A., Tyler, G.L., Zebker, H.A., Simpson, R.A., & Eshleman, V.R., 1983. Particle size distributions in Saturn's rings from Voyager 1 radio occultation. Icarus 54, 189-211.

Meinke, B.K., Esposito, L.W., Albers, N., & Sremčević, M., 2012. Classification of F ring features observed in Cassini UVIS occultations. Icarus 218, 545-554.

Michikoshi, S., & Kokubo, E., 2011. Formation of a propeller structure by a moonlet in a dense planetary ring. Astrophys. J. 732, L23-L26

Morishima, R., & Salo, H., 2004. Spin rates of small moonlets embedded in planetary rings. I. Three-body calculations. Icarus 167, 330-346.

Morishima, R., & Salo, H., 2006. Simulations of dense planetary rings. IV. Spinning self-gravitating particles with size distribution. Icarus 181, 272-291.

Nakazawa, K., & Ida, S., 1988. Hill's approximation in the three-body problem. Prog. Theoret. Phys. Suppl. 96, 167-174.

Nakazawa, K., Ida, S., & Nakagawa, Y., 1989. Collisional probability of planetesimals revolving in the solar gravitational field. Astron. Astrophys. 220, 293-300.

Nicholson, P.D., French, R.G., Tollestrup, E., Cuzzi, J.N., Harrington, J., Mathews, K., Perkovic, O., & Stover, R.J., 2000. Saturn's rings I. Optical depth profiles from the 28 Sgr occultation. Icarus 145, 474-501.

Ohtsuki, K. 1993. Capture probability of colliding planetesimals: Dynamical constraints on accretion of planets, satellites, and ring particles. Icarus 106, 228-246.

Ohtsuki, K. 1999. Evolution of particle velocity dispersion in a circumplanetary disk due to inelastic collisions and gravitational interactions. Icarus 137, 152-177.

Ohtsuki, K., 2005. Rotation rates of particles in Saturn's rings. Astrophys. J. 626, L61-L64.

Ohtsuki, K., 2006a. Rotation rate and velocity dispersion of planetary ring particles with size distribution. I. Formulation and analytic calculation. Icarus 183, 373-383.

Ohtsuki, K., 2006b. Rotation rate and velocity dispersion of planetary ring particles with size distribution. II. Numerical simulation for gravitating particles. Icarus 183, 384-395.

Ohtsuki, K. 2012. Collisions and gravitational interactions between particles in planetary rings. Prog. Theoret. Phys. Suppl. 195, 29-47.

Ohtsuki, K., & Emori, H., 2000. Local N-body simulations for the distribution and evolution of particle velocities in planetary rings. Astron. J. 119, 403-416.

Ohtsuki, K., & Toyama, D., 2005. Local N-body simulations for the rotation rates of particles in planetary rings. Astron. J. 130, 1302-1310.

Ohtsuki, K., Yasui, Y., & Daisaka, H., 2013. Accretion rates of moonlets embedded in circumplanetary particle disks. Astron. J. 146, 25.

Pollack, J.B., 1975. The rings of Saturn. Space Sci. Rev. 18, 3-93.

Pollack, J.B., Summers, A., & Baldwin, B., 1973. Estimates of the sizes of the particles in the rings of Saturn and their cosmogonic implications. Icarus 20, 263-278.

Porco, C.C., Thomas, P.C., Weiss, J.W., & Richardson, D.C., 2007. Saturn's small inner satellites: Clues to their origins. Science 318, 1602-1607.

Richardson, D.C., 1994. Tree-code simulations of planetary rings. Mon. Not. R. Astron. Soc. 269, 493-511.

Robbins, S.J., Stewart, G.R., Lewis, M.C., Colwell, J.E., & Sremčević, M., 2010. Estimating the masses of Saturn's A and B rings from high-optical depth N-body simulations and stellar occultations. Icarus 206, 431-445.

Salmon, J., Charnoz, S., Crida, A., & Brahic, A., 2010. Long-term and large-scale viscous evolution of dense planetary ring. Icarus 209, 771-785.

Salo, H., 1987. Numerical simulations of collisions between rotating particles. Icarus 70, 37-51.

Salo, H., 1992. Gravitational wakes in Saturn's rings. Nature 359, 619-621.

Salo, H., 1995. Simulations of dense planetary rings. Icarus 117, 287-312.

Salo, H., Schmidt, J., & Spahn, F., 2001. Viscous overstability in Saturn's B-ring: I. Direct simulations and measurement of transport coefficients. Icarus 153, 295-315.

Salo, H., Karjalainen, R., & French, R.G., 2004. Photometric modeling of Saturn's rings. II. Azimuthal asymmetry in reflected and transmitted light. Icarus 170, 70-90.

Schmidt, J., Ohtsuki, K., Rappaport, N., Salo, H., & Spahn, F., 2009. Dynamics of Saturn's dense rings. In: Dougherty, M.K., Esposito, L.W., Krimigis, S.M. (Eds.), Saturn from Cassini-Huygens. Springer, pp. 413-458.

Seiß, M., Spahn, F., Sremčević, M., & Salo, H. 2005. Structures induced by small moonlets in Saturn's rings: Implications for the Cassini Mission. Geophys. Res. Lett. 32. CiteID L11205.

Spahn, F., & Sremčević, M., 2000. Density patterns induced by small moonlets in Saturn's rings? Astron. Astrophys. 358, 368-372.

Sremčević, M., Spahn, F., & Duschl, W.J., 2002. Density structures in perturbed thin cold disks. Mon. Not. R. Astron. Soc. 337, 1139-1152.

Sremčević, M., Schmidt, J., Salo, H., Seis, M., Spahn, F., & Albers, N. 2007. A belt of moonlets in Saturn's A ring. Nature 449, 1019-1021.

Sremčević, M., Stewart, G., Albers, N., & Esposito, L.W., 2011. American Geophysical Union, Fall Meeting 2011, abstract P13B-1677.

Stewart, G.R., Lin, D., & Bodenheimer, P., 1984. Collision-induced transport processes in planetary rings. In: Greenberg, R., Brahic, A. (Eds.), Planetary Rings. Univ. of Arizona Press, Tucson, pp. 447-512.

Takeda, T., & Ida, S., 2001. Angular momentum transfer in a protolunar disk. Astrophys. J. 560, 514-533.

Tanaka, H., Ohtsuki, K., & Daisaka H. 2003. A new formulation of the viscosity in planetary rings. Icarus 161, 144-156.

Thomas, P.C., 2010. Sizes, shapes, and derived properties of the saturnian satellites after Cassini nominal mission. Icarus 208, 395-401

Tiscareno, M.S., Burns, J.A., Hedman, M.M., & Porco, C.C., 2008. The population of propellers in Saturn's A ring. Astrophys. J. 135, 1083-1091.

Tiscareno, M.S., Burns, J.A., Hedman, M.M., Porco, C.C., Weiss, J.W., Dones, L., Richardson, D.C., & Murray, C.D., 2006. 100-metre-diameter moonlets in Saturn's A ring from observations of 'propeller' structures. Nature 440, 648-650.

Tiscareno, M.S., Burns, J.A., Nicholson, P.D., Hedman, M.M., & Porco, C.C., 2007. Cassini imaging of Saturn's rings. II. A wavelet technique for analysis of density waves and other radial structure in the rings. Icarus 189, 14-34.

Tiscareno, M.S., Burns, J.A., Sremčević, M., Beurle, K., Hedman, M.M., Cooper, N.J., Milano, A.J., Evans, M.W., Porco, C.C., Spitale, J.N., & Weiss, J.W., 2010. Physical characteristics and non-keplerian orbital motion of "propeller" moons embedded in Saturn's rings. Astrophys. J. 718, L92-L96.

Tyler, G.L., Marouf, E.A., Simpson, R.A., Zebker, H.A., & Eshleman, V.R., 1983. The microwave opacity of Saturn's rings at wavelengths of 3.6 and 13 cm from Voyager 1 radio occultation. Icarus 54, 160-188.

Ward, W.R., & Cameron, A.G.W., 1978. Disc evolution within the Roche limit. In Proc. Lunar Planet. Sci. Conf., p. 1205 (abstract IX).

Weidenschilling, S.J., Chapman, C.R., Davis, D.R., & Greenberg, R., 1984. Ring particles: Collisional interactions and physical nature. In: Greenberg, R., Brahic, A. (Eds.), Planetary Rings. University of Arizona Press, Tucson, pp. 367-415.

Wisdom, J., & Tremaine, S., 1988. Local simulations of planetary rings. Astron. J. 95, 925-940.

Yasui, Y., Ohtsuki, K., & Daisaka, H., 2012. Viscosity in planetary rings with spinning self-gravitating particles. Astron. J. 143, 110

Yasui, Y., Ohtsuki, K., & Daisaka, H., 2014. Gravitational accretion of particles onto moonlets embedded in Saturn's rings. Astrophys. J., submitted.

Zebker, H.A., Marouf, E.A., & Tyler, G.L., 1985. Saturn's rings: Particle size distributions for thin-layer model. Icarus 64, 531-548.